iScience

CellPress
OPEN ACCESS

Article

# Strain-boosted hyperoxic graphene oxide efficiently loading and improving performances of microcystinase

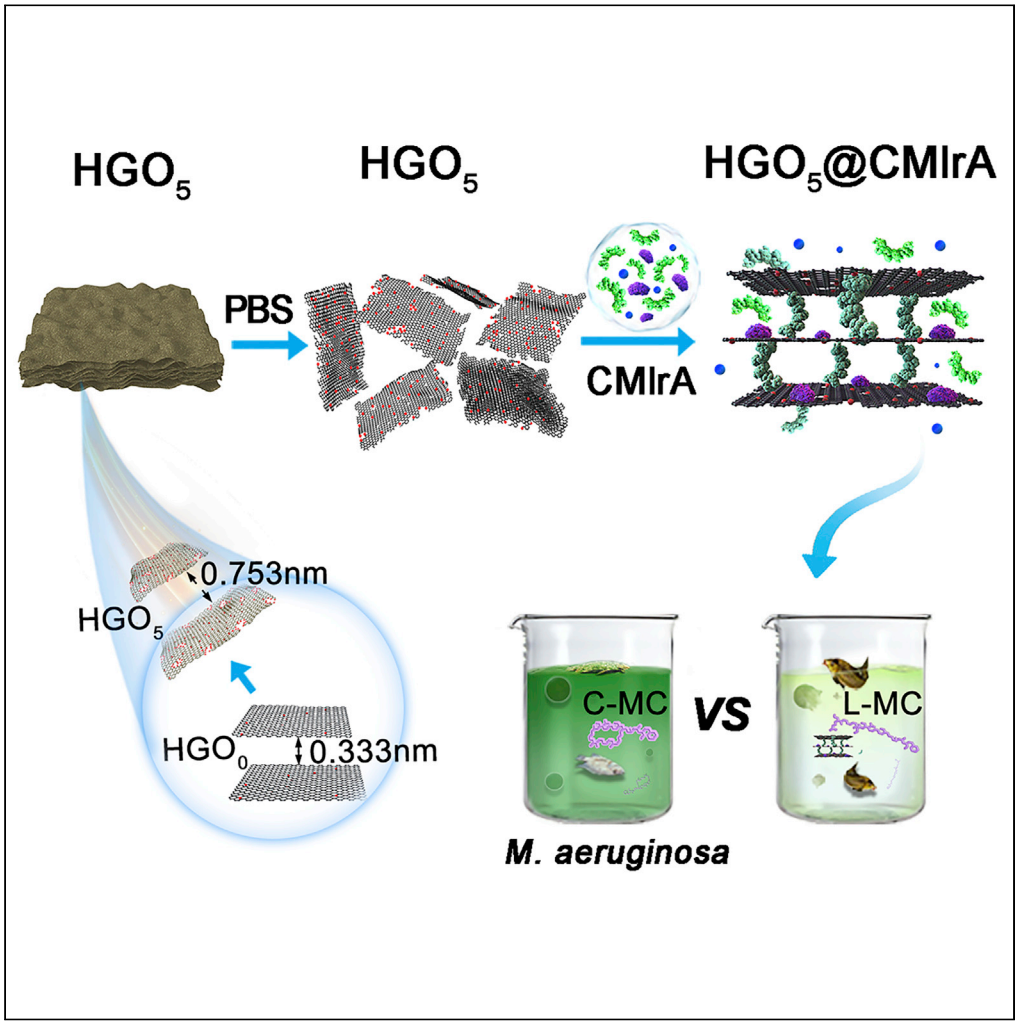


Hong-Lin Liu, Cai Cheng, Ling-Zi Zuo, ..., Yu Feng, Hai-Feng Qian, Ling-Ling Feng

hfqian@zjut.edu.cn (H.-F.Q.)
fll708@mail.ccnu.edu.cn (L.-L.F.)

## Highlights

Hyperoxic graphene oxide ($HGO_5$) provides inherent strain effects

$HGO_5$ exhibits an impressive loading capacity for MlrA

A new assembly mechanism for the $HGO_5$@MlrA composite is proposed

$HGO_5$@MlrA composite shows excellent capability and ecological safety

Liu et al., iScience 25, 104611
July 15, 2022 
https://doi.org/10.1016/j.isci.2022.104611

iScience

CellPress
OPEN ACCESS

Article

# Strain-boosted hyperoxic graphene oxide efficiently loading and improving performances of microcystinase

Hong-Lin Liu,[1,3] Cai Cheng,[1,3] Ling-Zi Zuo,[1,3] Ming-Yue Yan,[1] Yan-Lin He,[1] Shi Huang,[1] Ming-Jing Ke,[2] Xiao-Liang Guo,[1] Yu Feng,[1] Hai-Feng Qian,[2,*] and Ling-Ling Feng[1,4,*]

## SUMMARY

**Harmful *Microcystis* blooms (HMBs) and microcystins (MCs) that are produced by *Microcystis* seriously threaten water ecosystems and human health. This study demonstrates an eco-friendly strategy for simultaneous removal of MCs and HMBs by adopting unique hyperoxic graphene oxides (HGOs) as carrier and pure microcystinase A (PMlrA) as connecting bridge to form stable HGOs@MlrA composite. After oxidation, HGOs yield inherent structural strain effects for boosting the immobilization of MlrA by material characterization and density functional theory calculations. $HGO_5$ exhibits higher loading capacities for crude MlrA (1,559 mg·g$^{-1}$) and pure MlrA (1,659 mg·g$^{-1}$). Moreover, the performances of $HGO_5$@MlrA composite, including the capability of removing MCs and HMBs, the ecological and human safety compared to MlrA or $HGO_5$ treatment alone, have been studied. These results indicate that $HGO_5$ can be used as a promising candidate material to effectively improve the application potential of MlrA in the simultaneous removal of MCs and HMBs.**

## INTRODUCTION

The frequency and intensity of harmful *Microcystis* blooms (HMBs) are increasing globally, with HMBs and microcystins (MCs) produced by *Microcystis* contributing to the pollution of water environments and seriously threatening the health of animals and human beings. Cyanobacterial blooms frequently occurred in Taihu Lake, Dianchi Lake, and Chaohu Lake, the three largest lakes in China. In 2006, the area of blooms in China lakes was as high as 1363.3 km$^2$, decreased to 665.2 km$^2$ in 2013, but increased to 775.4 km$^2$ in 2018 (Huang et al., 2020; Huisman et al., 2018; Wang et al., 2021). Cyanotoxins were detected 1118 times in 869 freshwater ecosystems in 66 countries around the world, dating from the earliest records until 2018. And the detection frequency of MCs accounted for 63%, ranking the first (Svirčev et al., 2019). Several physical and chemical treatment strategies have been developed to efficiently alleviate HMBs, but these methods have some problems, including poor selectivity and difficulties in mitigating MCs release after cell lysis (Zhang et al., 2019a, 2019b; Li et al., 2011; Tsai et al., 2019; Feng et al., 2019). Microbial treatments are attractive alternatives but can bring potential risks owing to the secretion of unknown hazardous products (HPs) into water systems or by becoming new ecologically dominant species (Li et al., 2016; Yu et al., 2019). Consequently, the simultaneous and efficient removal of HMBs and MCs has become one of the most important issues in water resource pollution control.

Microcystinase A (MlrA) is the first and key enzyme involved in MCs biodegradation and has attracted extensive research attention owing to the potential for simultaneously removing HMBs and MCs for environmentally industrial application (Dexter et al., 2021; Liu et al., 2020). The cell-free crude enzyme extracts (CMlrA) from recombinant cells are analyzed in most studies (Dexter et al., 2021; Wang et al., 2017). Pure MlrA (PMlrA) was recently purified from CMlrA using commercial amylose-binding resins, as recently reported (Liu et al., 2020). Two types of MlrAs (CMlrA and PMlrA) have been obtained through heterologous expression and can simultaneously remove HMBs and MCs. However, the low activity yield of PMlrA and the unknown HPs in CMlrA are obstacles to the environmental or industrial application of MlrAs (Liu et al., 2020). Our preliminary studies demonstrated that the activity recovery rate of PMlrA was only 0.33% of that of CMlrA (Table S1). Therefore, the development of an optimized strategy to address both

[1]Key Laboratory of Pesticide & Chemical Biology (CCNU), Ministry of Education, College of Chemistry, Central China Normal University, Wuhan, 430079 Hubei Province, China

[2]College of Environment, Zhejiang University of Technology, Hangzhou, 310014 Zhejiang Province, China

[3]These authors contributed equally

[4]Lead contact

*Correspondence: hfqian@zjut.edu.cn (H.-F.Q.), fll708@mail.ccnu.edu.cn (L.-L.F.)

https://doi.org/10.1016/j.isci.2022.104611

activity yields and ecological security issues for the actual application of MlrAs to simultaneously remove HMBs and MCs remains a major challenge.

Graphene oxide (GO) nanomaterials have been widely used as promising treatments in many fields because they typically achieve considerably improved performances by tuning morphology, composition, and physicochemical properties (Chaudhary et al., 2021; Sun et al., 2021). However, the structural characteristics of GOs, including their functionalized molecules, microenvironments, and degree of oxidation, have important influences on their performance characteristics including their loading capability, stability, and potential toxicity (Chaudhary et al., 2021; Zhang et al., 2020a; Zolezzi et al., 2018). Our preliminary studies showed that several commercial GOs (CGOs) exhibited different carrying capacities for CMlrA (Table S2). The maximum loading amount of $CGO_3$ (monolayer GO) for CMlrA was notably observed with an approximately 18-fold higher capacity than the GO derivative modified with L-Cys (CysGO) which was the only GO derivative previously used to immobilize MlrA (Wu et al., 2020) (Table S1). Concomitantly, by using the crude maltose-binding protein (CMBP) from recombinant cells without the *mlr*A gene as control, the $CGO_3$@CMBP composite exhibited better safety than did $CGO_3$ or CMBP (Figure S1). Commercial monolayer GO ($CGO_3$) is expensive to generate, but these results suggest that it is possible to produce an appropriate GO nanomaterial that can improve the loading capacity of GO for CMlrA, while selectively removing HPs from CMlrA.

In this study, several GO derivatives were synthesized using a low-cost graphite powder. A hyperoxic graphene oxide ($HGO_5$) was successfully identified that exhibits impressively high loading capacities for MlrAs that are nearly comparable to these of $CGO_3$. The assembly mechanism of the $HGO_5$@CMlrA composite was further investigated using material characterization and density functional theory calculations. Furthermore, the $HGO_5$@CMlrA composites removed both HMBs and MCs. Lastly, the ecological safety of $HGO_5$@CMlrA composites was also evaluated. This study provides a promising and scalable paradigm whereby $HGO_5$ can be used as a potential nanomaterial to improve the application potential of MlrA in the simultaneous removal of MCs and HMBs.

## RESULTS AND DISCUSSION

### Characterization of structural strain effects of hyperoxic graphene oxides

Our preliminary experimental results indicated that higher total oxygen content (CTO) in CGOs was associated with higher loading capacities of CGOs for CMlrA (Table S2). Thus, their different immobilization performances could be related to their degree of oxidation (Tan et al., 2017; Zolezzi et al., 2018). To systematically explore the degree of oxidation on the immobilization performance of GO for MlrAs, nine types of HGOs ($HGO_1$-$HGO_9$) were prepared using $HGO_0$ as raw material and by altering the amount of added KMnO4 oxidant and the method of synthesis (M1 or M2) (Hummers and Offeman, 1958; Marcano et al., 2010) (Figures 1A and S2; Table S3). The loading capacities of HGOs for CMlrA were positively correlated with their total oxygen content ($C_{TO}$) when comparing HGOs prepared with the same raw material and synthesis method. For example, the loading capacity of $HGO_5$ for CMlrA (1,559 $mg \cdot g^{-1}$) was nearly five times higher than that of $HGO_0$ (303 $mg \cdot g^{-1}$), while the CTO of $HGO_5$ (46.4%) was nearly nine times higher than that for $HGO_0$ (5.05%) (Table S2). When varying the synthesis method, the loading capability of as-made HGOs for CMlrA significantly differed, even if their $C_{TO}$s were similar or identical. For example, the CMlrA loading amounts for $HGO_3$ and $HGO_7$ significantly differed (1,101 $mg \cdot g^{-1}$ and 791 $mg \cdot g^{-1}$, respectively) although their $C_{TO}$s were similar (35.4 and 37.5%, respectively). The effects of raw materials on GO loading capacities were also compared when using the same synthesis method. $ZGO_1$ was synthesized using the raw material $ZGO_0$ (Huang et al., 2019) which differed from $HGO_0$ because it used the same synthesis method as used for $HGO_5$. Accordingly, the $C_{TO}$s and the CMlrA-loading capacities of $ZGO_1$ and $HGO_5$ were significantly different (Table S2).

HGO functions were consequently hypothesized to not only be related to $C_{TO}$, but also to other structural changes that could have occurred during the oxidation process that then affected the binding of MlrA on HGOs. Strain effect is a commonly used comprehensive factor for evaluating structure-performance relationships in nanomaterial engineering (Li et al., 2020; Luo and Guo, 2017). Scanning electron microscopy (SEM) imaging revealed that the surface roughness and wrinkle degree of HGOs were gradually enhanced with increased $KMnO_4$ addition, indicating that the process of oxidation altered the surface properties of HGOs and clearly generated higher concentrations of lattice defects (Figures 1B and S3). Similar patterns have been observed in CGOs and ZGOs prepared from different sources (Figure S4). The lattice defects of

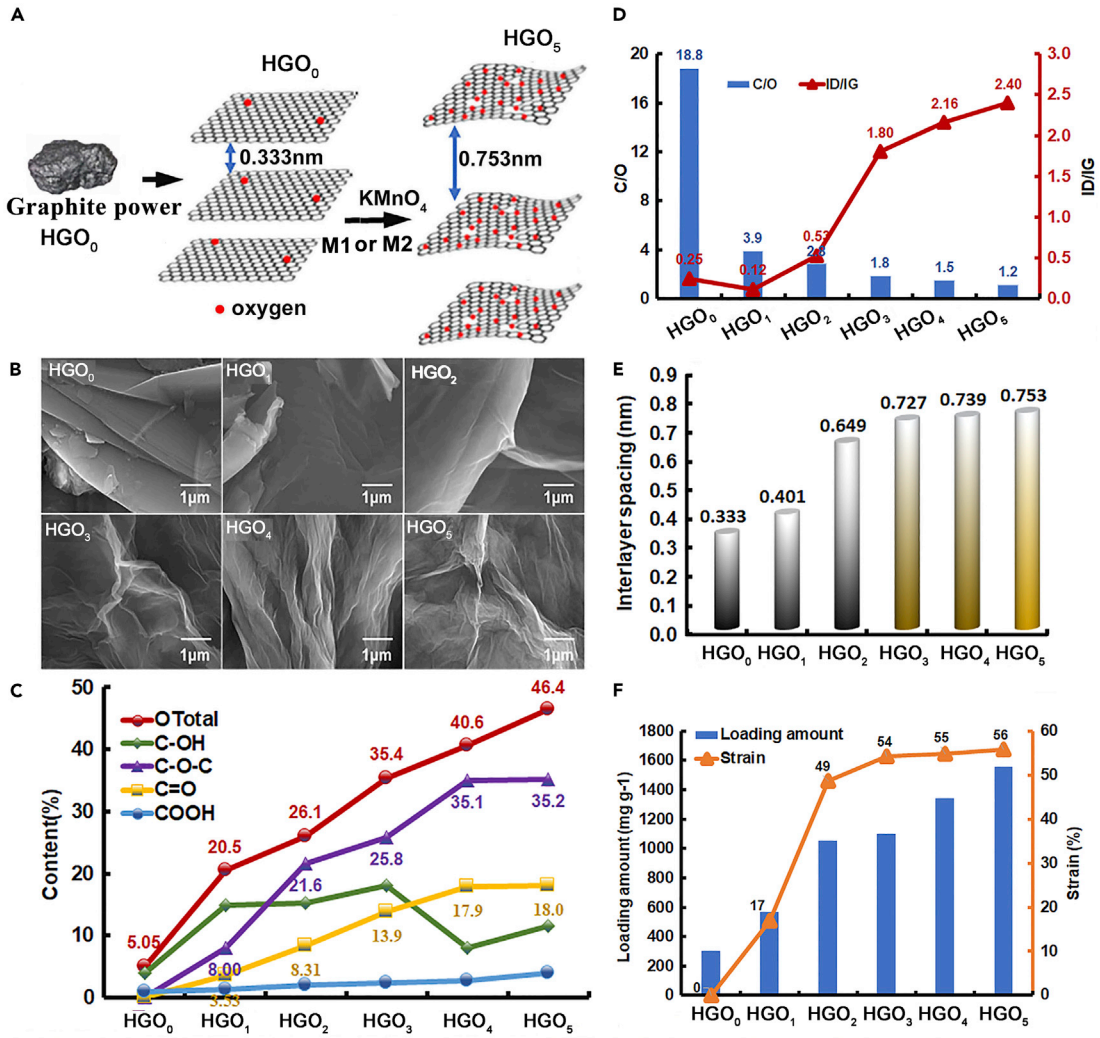


**Figure 1. Characterization of structural strain effects of HGOs ($HGO_1$-$HGO_5$)**

(A) Schematic showing the overall process of HGO preparation.

(B) Scanning electron microscopy (SEM) images.

(C) Total oxygen content and functional group contents of GOs.

(D) C/O and $I_D/I_G$ ratios.

(E) Average interlayer spacing.

(F) The loading capacities of HGOs for CMlrA in addition to HGO strain levels. $HGO_0$ is the graphite powder used as the raw material. Data are represented as mean ± SEM.

GOs might be attributable to the insertion of oxygen-containing groups that induce the internal structure and external morphology strain effects in GOs (Reynosa-Martínez et al., 2020; Tan et al., 2017).

X-ray diffraction (XRD) further revealed that a new peak at $2\theta = 10.7°$, corresponding to the crystal plane of GO (001), began to appear in $HGO_1$ or $HGO_6$, and then gradually increased from $HGO_1$ to $HGO_5$ or from $HGO_6$ to $HGO_9$ (Figures S5B and S6B). Concomitantly, the peak at $2\theta = 26°$ corresponding to the graphite crystal plane (002) became wider and then gradually decreased until it was not detected. These results suggested that HGOs were prepared by destroying C=C bonds and inserting different degrees of oxygen-containing functional groups into the graphite lattice of $HGO_0$, thereby resulting in more tensile strain effects (Li et al., 2020; Reynosa-Martínez et al., 2020; Tan et al., 2017). Similar patterns have been observed in CGOs and ZGOs prepared from different sources (Figure S7B). Furthermore, X-ray photoelectron spectroscopy (XPS) analysis demonstrated that the $O_{1S}$ peak gradually increased, while the $C_{1S}$ peak gradually decreased from $HGO_0$ to $HGO_5$ and from $HGO_6$ to $HGO_9$, indicating that increased $KMnO_4$ addition led to

gradual increases in the $C_{TO}$s of HGOs (Figures S5D and S6D). The $C_{TO}$ value of $HGO_5$ was up to nine times higher than that of $HGO_0$ (Table S2). Similar patterns have been observed in CGOs from different sources (Figure S7D). Moreover, high-resolution XPS analysis revealed that variation in several oxygen-containing functional group contents differed when comparing $HGO_0$ to $HGO_5$ or $HGO_6$ to $HGO_9$ (Figure 1C and Table S2, Figures S8 and S9) (Al-Gaashani et al., 2019). Similar differences were observed in CGOs and ZGOs prepared from different materials (Figure S10).

Raman spectroscopy (RS) imaging revealed that when HGO oxidation degree increased, their intensity ratio ($I_D/I_G$) and full width at half maximum (FWHM) values of the D to G bands also increased, while their C/O ratios decreased (Figures 1D and Table S4, Figures S5A and S6A). These results indicated the presence of increasing strain effects from $HGO_0$ to $HGO_5$ and from $HGO_6$ to $HGO_9$, consistent with the SEM characterizations (Reynosa-Martínez et al., 2020; Li et al., 2020). RS variation provides evidence that increasing levels of oxygen-containing functional groups were inserted into the carbon networks of the HGOs, resulting in unique structural strains among different HGOs that could then be modified to achieve desirable HGO properties (Reynosa-Martínez et al., 2020; Li et al., 2020). Similar differences were observed in CGOs prepared from different materials (Figure S7A).

Interestingly, increased HGO interlayer spacings were proportional to the oxidation degree owing to the intercalation of oxygen-containing functional groups in the contiguous aromatic lattices of $HGO_0$ such as epoxides, ketone carbonyls, and carboxylic groups (Figure 1E). The Bragg law indicated that the interlayer spacing between $HGO_5$ nanosheets induced a tensile strain rate ($S_{FGO5}$) of 126.1% compared to $HGO_0$ (Table S5). Furthermore, the strain effects were positively correlated with the HGO loading levels (Figure 1F). Moreover, Fourier Transform Infrared Spectroscopy (FTIR) analysis demonstrated that increased oxidation degree led to the appearance of different oxygen-containing functional groups in GOs (Figures S5C, S6C, and S7C). A significant band near 3,500 $cm^{-1}$ was identified corresponding to the stretching of the −OH functional group and hydrogen-bonded water (H-*O*-H), and gradually widened from $HGO_0$ to $HGO_5$ and from $HGO_6$ to $HGO_9$, indicating that the hydrophilicity of HGOs increased with increasing oxidation degree (Figures S5C and S6C).

It is worth noting that $HGO_1$ and $HGO_6$ were synthesized using the same oxidant (0.3 g $KMnO_4$) via M1 and M2, respectively, and the $C_{TO}$s of $HGO_1$ and $HGO_6$ were similar. However, their contents of oxygen-containing functional groups, interlayer spacing, and $I_D/I_G$ values were significantly different (Tables S2–S5). $HGO_3$ and $HGO_7$ also exhibited similar characteristics. Thus, HGOs, that were synthesized by different methods, even when prepared from the same raw material, may have different strain effects, leading to unique functional characteristics. Considering the same amount of oxidant, the HGOs synthesized via M1 produced more suitable structural strain effects for loading CMlrA than those produced via M2, as evaluated by loading capacities (Table S2).

In an aqueous solution (pH 7.4), the zeta potential gradually decreased from $HGO_0$ to $HGO_5$ and from $HGO_6$ to $HGO_9$, indicating that higher oxidation degrees led to more stable HGOs (Table S6). In solutions with pH values ranging from 5.3 to 9.3, $HGO_5$ zeta potentials were lower than those of $HGO_0$, indicating that a high degree of oxidation in $HGO_5$ led to greater stability than $HGO_0$ over a wider pH range (Table S6). The stabilities of HGOs in aqueous solutions can be attributed to the concentration of oxygenated functional groups and the dissociation of acid functional groups such as carboxylic acid ($-COO^- + H^+$) and hydroxyl ($OH^-$) groups (Reynosa-Martínez et al., 2020; Zolezzi et al., 2018).

Combined with the structural characterizations discussed above, the oxidation of $HGO_0$ resulted in distinct strain effects owing to the introduction of oxygen. The strain effects of HGOs were positively correlated with their $C_{TO}$s, but also included changes in other characteristics such as lattice morphology, oxygen-containing group composition, interlayer spacing, and electronegativity. Consequently, strain effects may optimize the performance of HGOs for effective combination with CMlrA, resulting in greater strain that then leads to higher loading capacities of HGOs for CMlrA (Figure 1F) (Li et al., 2020; Zhang et al., 2014; Luo and Guo, 2017).

## Structural characterization of the HGO5@CMlrA composite

To investigate the role of HGO strain effects in promoting combination with CMlrA, $HGO_5$ was used as an exemplary material to prepare the $HGO_5$@CMlrA composite using physical adsorption and covalent

binding methods (Table S1). Physical adsorption is widely used for enzyme immobilization because it is typically simple to conduct and minimally affects enzyme activity. Covalent binding generally leads to higher loading capacity and stability of nanomaterials than physical adsorption, although it may be a more complex process and considerably affects enzyme activities (Zhuang et al., 2020; Monajati et al., 2018; Chaudhary et al., 2021). The assembly conditions of the two methods for the $HGO_5$@CMlrA composites were also optimized (Figures S11 and S12). Under optimal conditions, the loading capacity of $HGO_5$ for CMlrA increased up to 1,654 $mg \cdot g^{-1}$ with the covalent cross-linking method, which was slightly higher than that achieved with the adsorption method (1,559 $mg \cdot g^{-1}$) (Table S1). In contrast, the loading capacity of $HGO_5$ for PMlrA increased by up to 1,659 $mg \cdot g^{-1}$ when prepared using the adsorption method, representing a slightly higher value than that of CMlrA with the same method (1,559 $mg \cdot g^{-1}$). These results indicated that $HGO_5$ can efficiently load MlrAs when prepared by both adsorption and covalent methods, representing much higher values than that achieved with L-CysGO (89.77 $mg \cdot g^{-1}$) (Wu et al., 2020) (Table S1). The adsorption method allowed easy control of high loading performance conditions and thus, the $HGO_5$@CMlrA used in subsequent studies was prepared by the adsorption method unless otherwise indicated.

FTIR spectroscopy revealed a characteristic N-H peak (1,536 $cm^{-1}$) for $HGO_5$@CMlrA, indicating that CMlrA was successfully loaded onto $HGO_5$ (Figure 2A). C-*O*-C antisymmetric tensile vibration bands (1,220 $cm^{-1}$) were observed in both the $HGO_5$ and $HGO_5$@CMlrA, corresponding to the characteristic peaks for C=C (1,616 $cm^{-1}$), C=O (1,720 $cm^{-1}$), -OH, (3,500 $cm^{-1}$), as previously reported in other studies (Zhuang et al., 2020; Chaudhary et al., 2021). Thus, most of the functional groups and the skeleton structure of $HGO_5$ were not damaged after CMlrA immobilization.

In addition, XRD analysis revealed that the characteristic diffraction peak of the GO (001) crystal plane at 2θ of 10.7° in $HGO_5$@CMlrA disappeared and an amorphous peak appeared at 2θ of 20-30° that may be caused by crystal structure changes of $HGO_5$ immobilizing CMlrA (Figure 2B). Specifically, the energy-dispersive X-ray spectroscopy (EDS) analysis revealed that the corresponding N element mapping of $HGO_5$@CMlrA was obviously higher than that of $HGO_5$, further confirming that $HGO_5$@CMlrA was successfully prepared (Figure 2D) (Zhuang et al., 2020; Chaudhary et al., 2021). Fluorescein isothiocyanate (FITC)-labeled CMlrA (F-CMlrA) and $HGO_5$@F-CMlrA exhibited higher fluorescence intensities, while $HGO_5$ and CMlrA did not exhibit any measurable fluorescence intensity (Figure S13). Fluorescence confocal scanning electron microscopy (FCSEM) visually confirmed that F-CMlrA was successfully loaded onto $HGO_5$ surfaces (Figure S14).

The above results indicated that the $FGO_5$@MlrA composite was successfully prepared. However, SEM observations indicated that the lamellar thickness of $HGO_5$@CMlrA was clearly greater than that of $HGO_5$ (Figure S15). RS spectroscopy also revealed that the $I_D/I_G$ and FWHM values of $HGO_5$@CMlrA were higher than those of $HGO_5$, indicating that the loading of CMlrA on $HGO_5$ further increased $HGO_5$ strain (Figures 2C and Table S4) (Chaudhary et al., 2021; Marcana et al., 2010; Krishnamorthy et al., 2013). Moreover, when comparing materials prepared using the same adsorption synthesis method, the loading capacity of $HGO_5$ for CMlrA (up to 1,559 $mg \cdot g^{-1}$) was 17 times higher than that of CysGO (89.77 $mg \cdot g^{-1}$) (Wu et al., 2020). The loading capacities were also significantly higher than those of other modified GO derivatives for their respective enzymes (e.g., Glu-r3h-GO for lipase and PEGA-GOMNP for xylanase, 217 $mg \cdot g^{-1}$ and 273 $mg \cdot g^{-1}$, respectively) (Zhuang et al., 2020; Mehnati-Najafabadi et al., 2018), and also five times higher than that of $HGO_0$ (303 $mg \cdot g^{-1}$) (Tables S1 and S2). These results suggest that the $HGO_5$@CMlrA composite may be assembled through a new mechanism differing from that of other modified GO derivatives that simply absorb enzymes on their surfaces (Zhuang et al., 2020; Mehnati-Najafabadi et al., 2018; Wu et al., 2020).

## Assembly mechanism of the HGO5@CMlrA composite

GOs have been recently reported to be easily dispersed into monolayer GO nanosheets in aqueous solutions and these dispersed single-layer GO nanosheets can then be reconstituted into multilayer GO nanomaterials by molecular crosslinking. (Zhang et al., 2020a; Chen et al., 2017). Both $CGO_3$ (a monolayer GO) and $HGO_5$ exhibited impressively high carrying capacities for CMlrA (Table S2). Consequently, a new assembly mechanism of the $HGO_5$@CMlrA composite was proposed here that involves $HGO_5$ being dispersed to form monolayer GOs in the aqueous solution, followed by CMlrA acting as a molecular bridge to re-assemble the dispersed monolayer GO to form the $HGO_5$@CMlrA composite catalyst (Figure 3A). In contrast, $HGO_0$ maintains a multilayer configuration in the aqueous solution and primarily absorbs CMlrA on its surface (Figure 3B).

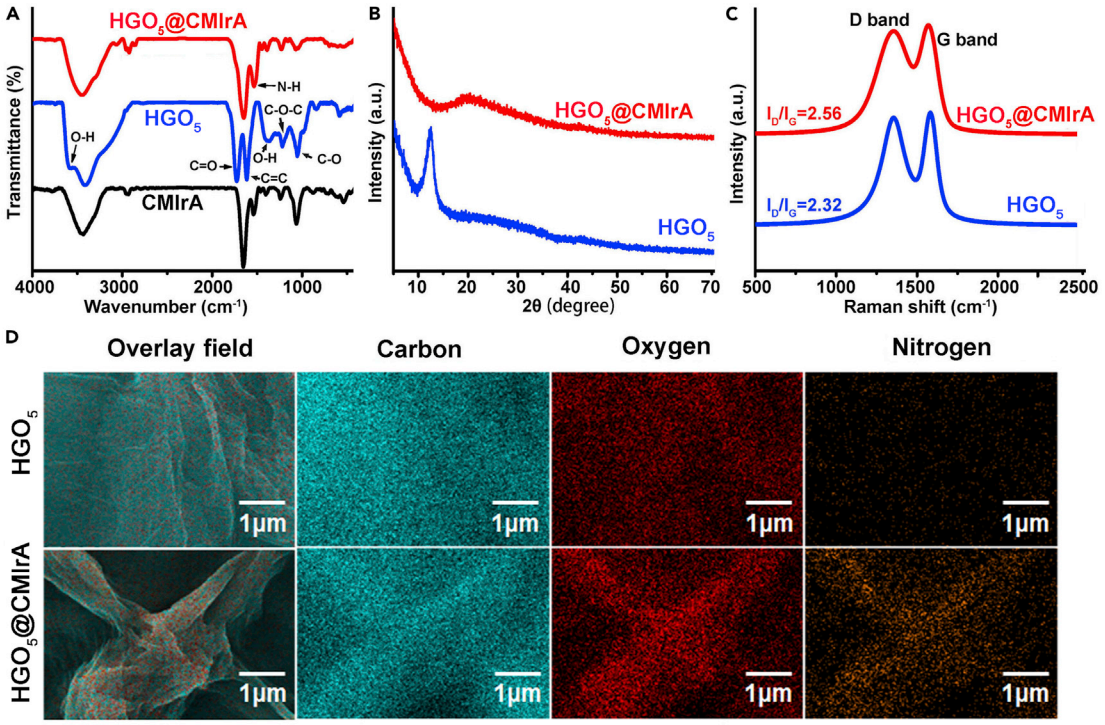


**Figure 2. Chemical characterization of $HGO_5$@CMIrA**

(A) Fourier transform infrared spectroscopy (FTIR) images.

(B) X-ray powder diffraction (XRD) images.

(C) Raman spectroscopy (RS) images.

(D) Energy dispersive X-ray spectroscopy (EDS) images.

The interlayer spacing of $HGO_5$ was only 0.753 nm, which is not large enough for CMIrA to enter the $HGO_5$ interlayers (Table S5). AFM imaging was used to validate the proposed assembly mechanism of $HGO_5$@CMIrA (Figures 3C and 3D). Compared to $HGO_0$, the $HGO_5$ lamellae were very irregular and the transparency of graphene layers in $HGO_5$ was much higher than in $HGO_0$. $HGO_5$ thickness (about 1.1 nm) was equivalent to an $HGO_5$ monolayer, while the thickness of $HGO_5$@CMIrA increased to around 6-12 nm (equivalent to 8-16 layers of $HGO_5$) owing to the interlayer spacing of $HGO_5$ (0.753 nm) (Figure 3C). In contrast, $HGO_0$ with a thickness of about 20-30 nm is equivalent to 60-90 layers of $HGO_0$ lamellae, while the thickness of $HGO_0$@CMIrA decreased to around 10-12 nm owing to the interlayer spacing of $HGO_0$ (0.333 nm) (Figure 3D). GOs can be dispersed into monolayer GO in the aqueous solution (Zhang et al., 2020a; Klechikov et al., 2015; Sun et al., 2016; Chen et al., 2017). After the addition of CMIrA, dispersed monolayer GO incorporated CMIrA as a connecting bridge, leading to reconstitution into multilayer GO owing to the interactions between CMIrA and monolayer GO. At this stage, the $HGO_5$@CMIrA composite was successfully and efficiently assembled, resulting in a significantly high loading capacity for CMIrA (Figure 3A). In contrast, $HGO_0$ was difficult to disperse into monolayers and remained in a multilayer configuration within the aqueous solution. Consequently, CMIrA was only assembled on the surface of multilayer $HGO_0$, resulting in a low loading capacity for CMIrA, as observed elsewhere (Figure 3B) (Zhuang et al., 2020; Mehnati-Najafabadi et al., 2018; Wu et al., 2020).

The assembly process of the $HGO_5$@CMIrA composite highly depends on the surface electronegativity of $HGO_5$. Thus, the density functional theory (DFT) calculation was used to analyze the theoretical rationality of the assembly model of the $HGO_5$@CMIrA composite (Figures 3E and 3F) (Lu and Chen, 2012; Humphrey et al., 1996). The overall average surface electrostatic potential (ESP) value of $HGO_5$ (−5.41 eV) was much lower than that of $HGO_0$ (−0.006 eV), indicating that $HGO_5$ had stronger electronegativity than $HGO_0$. Moreover, the penetration distance between $HGO_5$ and CMIrA (3.97 Å) was much higher than that between $HGO_0$ and CMIrA (0.90 Å), suggesting that the binding ability of $HGO_5$ for CMIrA was much stronger than that of $HGO_0$ in $HGO_0$@CMIrA.

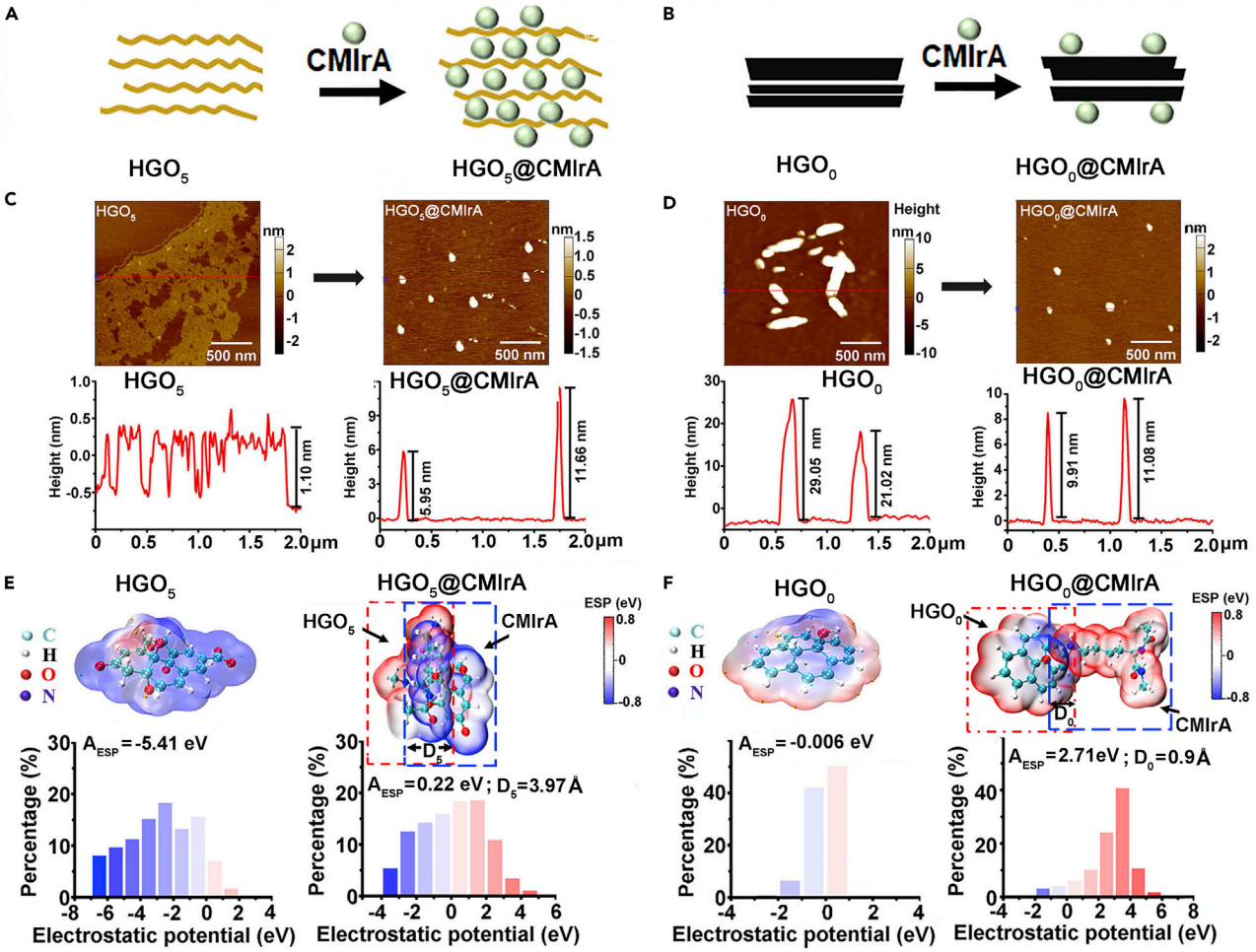


**Figure 3. Preparation of $HGO_5$@CMIrA and its assembly mechanism**

(A and B) Schematics for $HGO_5$@CMIrA and $HGO_0$@CMIrA assembly, respectively.

(C and D) Atomic force microscopy (AFM) images of $HGO_5$@CMIrA and $HGO_0$@CMIrA, respectively.

(E and F) Density functional theory (DFT) calculations for $HGO_5$@CMIrA and $HGO_0$@CMIrA, respectively. Blue indicates negative potential and red indicates positive potentials.

To confirm the effects of the pH of the reaction solution and the electronegativity of the material on the assembly of $HGO_5$ and CMIrA, $HGO_5$ was further modified with amino groups to obtain $HGO_5$-$NH_2$. The potential value of $HGO_5$-$NH_2$ was higher than that of $HGO_5$, resulting in a 12.8-fold decrease in CMIrA loading on $HGO_5$-$NH_2$ (i.e., only 122 $mg \cdot g^{-1}$) (Table S7). Under assembly conditions of pH 7.4 and 30 min of assembly time, the loading amount of CMIrA by $HGO_5$ reached equilibrium at a loading capacity up to 1,559 $mg \cdot g^{-1}$ (Figure S11), while that of $HGO_5$ for PMIrA reached 1,659 $mg \cdot g^{-1}$ (Table S1), representing a roughly 20-fold increase over previous reports of Cys-GO for PMIrA (Wu et al., 2020). These results further confirmed that $HGO_5$ combined with CMIrA to assemble the $HGO_5$@CMIrA composite via a novel mechanism different than those established in previous reports. (Zhuang et al., 2020; Mehnati-Najafabadi et al., 2018; Wu et al., 2020). In addition, the leakage rates of $HGO_5$@CMIrA obtained owing to adsorption and covalent methods were less than 11% after incubating in different pH buffers for 60 min. Moreover, almost no leakage was observed at pH 7.4, even if the leakage rate was less than 12% at pH 10.5 after 8 h of incubation (Table S8). These results indicated that $HGO_5$ can reconstruct a stable $HGO_5$@CMIrA composite using CMIrA as a molecular bridge by adsorption.

The experiments described above confirmed the novel assembly mechanism of the $HGO_5$@CMIrA composite when using $HGO_5$ combined with CMIrA. All of these factors, including high oxygen and oxygen-containing functional group content, enlargement of interlayer spacing, and enhanced electronegativity

combined to form sufficient strain effects for dispersing $HGO_5$ into monolayer GO in aqueous solution, are hypothesized to result in increased numbers of free $HGO_5$ monolayers, while also exposing abundant binding sites, leading to stronger electronegativity that would immobilize CMlrA (Tables S2 and S6). Subsequently, interactions between CMlrA and monolayer GO would promote the formation of the stable $HGO_5$@CMlrA composite (Zolezzi et al., 2018; Li et al., 2020; Zhang et al., 2014., Wang et al., 2011). This mechanism could explain the high loading capacity of $HGO_5$ for CMlrA and the assembly of a stable $HGO_5$@CMlrA composite.

## The catalytic performances of the $HGO_5$@CMlrA composite

$HGO_5$@CMlrA exhibited efficient degradation activities against the three most common MCs (Figure S16) and had the same degradation product (Figure S17), consistent with the free enzymes CMlrA and PMlrA (Liu et al., 2020), indicating that not only degradation product pathway by $HGO_5$@CMlrA composite is the same as that of MlrA, but also CMlrA activity was better maintained after cross-linking with $HGO_5$ nanosheets. The oxygen-containing functional groups on $HGO_5$ facilitated the adsorption of MC-LR on the surface of $HGO_5$ through interactions such as electrostatic interactions, hydrophobic interaction, $\pi$-$\pi$ interactions, and hydrogen bonds (Zeng and Kan, 2021). MC-LR is gathering on the surface of $HGO_5$@CMlrA, which makes MC-LR more accessible to CMlrA and hydrolyzed to chain MC-LR by CMlrA. Notably, the activity recovery rate of $HGO_5$@CMlrA from CMlrA significantly increased to 46.3%, which was 140 times higher than that of PMlrA from CMlrA (Table S1).

The degradation activity of $HGO_5$@CMlrA toward MC-LR was almost as high as that of free CMlrA after 1 h (Figure S18). The results showed that the degradation activities of $HGO_5$@CMlrA and free CMlrA toward MC-LR are time-dependent. The adsorption of the substrate (MC-LR) on $HGO_5$ reached equilibrium within 5 min and a maximum adsorption rate of 32.5% was observed. The potential mechanism of MC removal by $HGO_5$@CMlrA composite was owing to the catalytic activity of $HGO_5$@CMlrA composite, not owing to the adsorption of the substrate (MC-LR) on $HGO_5$.

The effect of substrate or enzyme concentration on the degradation activities of $HGO_5$@CMlrA was investigated (Figure S19). The enzymatic reaction is a first-order reaction when the concentration of MC-LRwas low and it was transitioned to zero-order reaction as the concentration of MC-LR increased. Furthermore, the calculation of Michaelis constant ($K_m$) and maximum reaction velocity ($V_{max}$) values of $HGO_5$@CMlrA indicate that the binding capacity of $HGO_5$@CMlrA to MC-LR was slightly lower than that of free CMlrA to MC-LR, while the specific activity of CMlrA was well-maintained after being immobilized on $HGO_5$ (Figures S19A and S19B). Degradation activities of $HGO_5$@CMlrA and free CMlrA toward MC-LR were concentration-dependent (Figure S19C).

The stability of $HGO_5$@CMlrA catalytic activity is also an important factor requiring evaluation. The results of structure characterization showed that the skeleton of $HGO_5$@CMlrA did not damage and $HGO_5$ was slightly reduced in the process of MC-LR degradation (Figure S20). $HGO_5$@CMlrA outperformed free CMlrA because it maintained more of its initial catalytic activities than free CMlrA under various adverse conditions (Figure S21). Specifically, the alkali tolerance of $HGO_5$@CMlrA was particularly significantly improved (Figure S21B). This could be attributed to the formation of microenvironments within $HGO_5$ that hindered the destruction of the conformation and the active site of the enzyme owing to pH stress (Chaudhary et al., 2021). As water pH can range up to about 10.5 during HMBs, the strong alkali resistance of $HGO_5$@CMlrA renders it more useful than CMlrA for controlling HMB and MCs pollution. The storage stability of enzymes is an important metric to evaluate the potential for their industrial application. The half-life of CMlrA was 10 days, while the half-life of $HGO_5$@CMlrA was up to 24 days at 4 °C, indicating significantly higher storage stability of $HGO_5$@CMlrA compared to that of CMlrA (Figure S21C). Therefore, the application of $HGO_5$@CMlrA could effectively be conducted at low cost, while maintaining catalytic activity over time.

## Effective inhibition of $HGO_5$@CMlrA on *M. aeruginosa*

The effects of $HGO_5$@CMlrA concentrations and treatment time on the inhibition of *Microcystis aeruginosa* (*M. aeruginosa*) were studied (Figure S22). It was shown that the inhibition rates of $HGO_5$@CMlrA against the growth of *M. aeruginosa* were time-dependent and concentration-dependent (Figure S22). The inhibition activity of $HGO_5$@CMlrA against *M. aeruginosa* was similar to that of free CMlrA and PMlrA, reaching 85.7% after nine days of treatment (Figure S23) (Liu et al., 2020). $HGO_5$ treatment also exhibited negative effects on *M. aeruginosa* cell growth, with an inhibitory rate of about 28.7%.

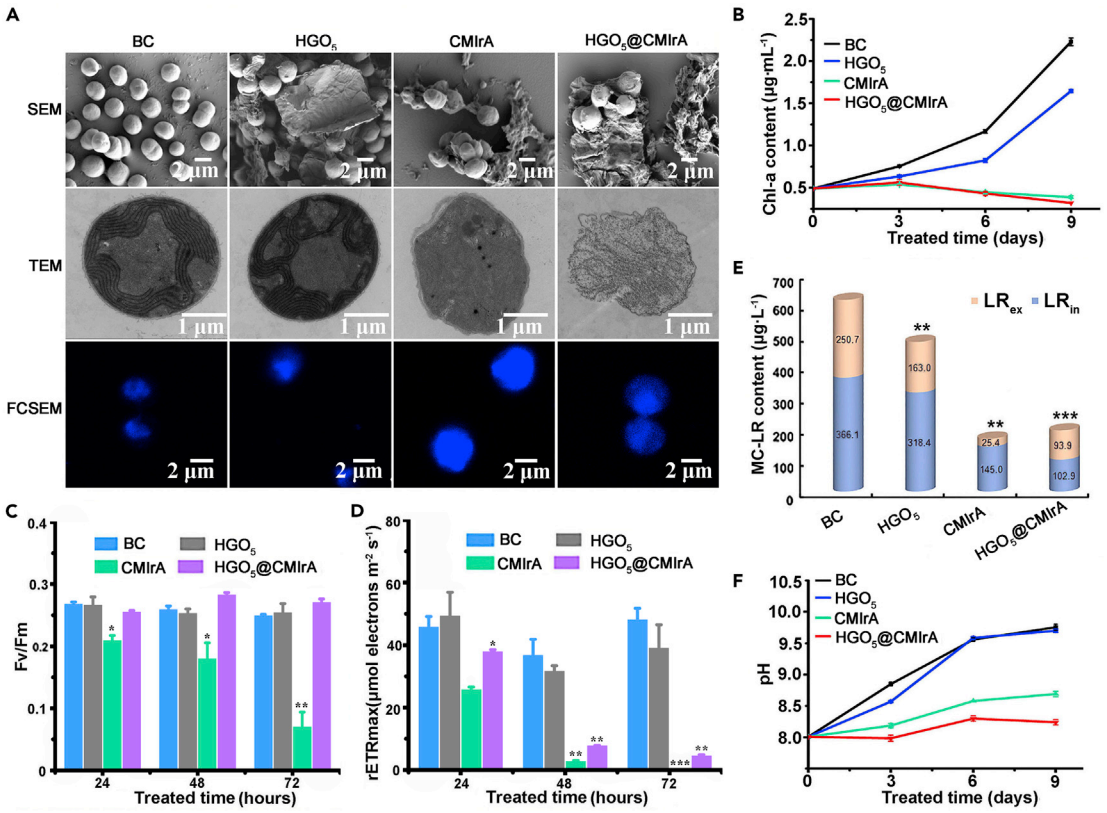


**Figure 4. The effects of $HGO_5$@CMIrA treatment on *M. aeruginosa* cells**

(A) Cell morphology observations using scanning electron microscopy (SEM), transmission electron microscopy (TEM), and fluorescence confocal scanning electron microscopy (FCSEM).

(B) Chlorophyll *a* (Chl-a) contents.

(C and D) The maximum quantum yields of photosystem II ($F_v/F_m$); (D) The maximum relative electron transfer rates ($rETR_{max}$).

(E) Intercellular MC-LR ($LR_{in}$) and extracellular MC-LR ($LR_{ex}$) contents.

(F) Culture pH at different days. BC indicates the control group.

Asterisks (*, **, and ***) represent statistically significant differences compared to controls ($p < 0.05$, $p < 0.01$, and $p < 0.001$, respectively; $n = 3$). Data are represented as mean ± SEM.

The *M. aeruginosa* was disrupted by $HGO_5$@CMIrA and turned into environmentally friendly organisms that can provide nutrients for the growth of other aquatic organisms (Hadi and Brightwel, 2021). Compared to control group *M. aeruginosa* cells (BC), $HGO_5$@CMIrA and CMIrA group cells all exhibited wrinkling or ruptures, plasmolysis, cell content overflowing, and cell organelle damage, indicating that both $HGO_5$@CMIrA and CMIrA could destroy cellular nucleoid regions. However, the effects of $HGO_5$@CMIrA treatment on cells were more serious (Figure 4A). Cells after $HGO_5$ treatment remained smooth and spherical, although some intracellular changes began to occur, indicating that $HGO_5$ treatment led to adverse effects on *M. aeruginosa* cells. Thus, the destruction of *M. aeruginosa* cells by $HGO_5$@CMIrA may result from the synergistic activities of CMIrA and $HGO_5$, resulting in greater damage to cells than from either component alone.

Chl-a is typically measured to reflect the photosynthetic capacity of *M. aeruginosa* cells. Chl-a content in the $HGO_5$@CMIrA treatment group cells was similar to that observed for the CMIrA treatment, but lower than that in the PMIrA treatment. In contrast, $HGO_5$ exhibited slightly negative effects on Chl-a content, indicating that $HGO_5$@CMIrA and CMIrA treatment led to greater effects on Chl-a than did PMIrA and $HGO_5$ (Figure 4B) (Liu et al., 2020). *Fv/Fm* and rETRmax are two commonly used parameters for evaluating photosynthetic activity. *Fv/Fm* represents the maximum quantum conversion efficiency of photosynthetic system II (PSII), while $rETR_{max}$ represents the maximum electron transfer rates of PSII. Investigation of these changes in photosynthetic systems revealed that $HGO_5$@CMIrA exhibited no significant effect on $F_v/F_m$, similar to the $HGO_5$ treatment, but had lesser impacts on $rETR_{max}$ than did the CMIrA treatment (Figures 4C and 4D).

The genetic regulatory mechanisms underlying photosynthesis in *M. aeruginosa* were also studied via their transcriptional responses to $FGO_5$@CMlrA exposure (Figure S24). *psa*B, *psb*D, and *rbc*L are involved in the photosynthesis pathway. *psa*B encodes the reaction center subunit of PSI. *psb*D encodes the D2 protein of the PSII reaction center. *rbc*L encodes the ribulose-1,5-bisphosphate large subunit that is critical for the Calvin cycle. $FGO_5$@CMlrA had obvious inhibitory effects on the transcription levels of *psa*B and *rbc*L (Figure S24A). However, $HGO_5$@CMlrA did not significantly affect the transcription levels of *psb*D, while CMlrA significantly inhibited *psb*D (Liu et al., 2020). Both $HGO_5$@CMlrA and CMlrA treatment effectively degraded total MCs. $HGO_5$@CMlrA treatment was more effective in degrading intercellular MCs ($LR_{in}$) while CMlrA treatment was more effective in degrading extracellular MCs ($LR_{ex}$) (Figure 4E). $HGO_5$@CMlrA significantly inhibited the transcriptional level of genes in the MC-LR synthesis pathway including *mcy*B, *mcy*D, and *mcy*G (Figure S24B), even more so than by PMlrA treatment (Liu et al., 2020). These results suggest that decreased expression of MC-LR synthesis pathway genes may lead to the reduction of $LR_{in}$ levels under $HGO_5$@CMlrA treatment, consistent with the $LR_{in}$ measured above (Figure 4E). In addition, $HGO_5$@CMlrA treatment led to better maintenance of a weakly alkaline environment than did CMlrA treatment, while $HGO_5$ treatment alone did not affect culture pH (Figure 4F). The skeleton of $HGO_5$@CMlrA was not significantly damaged with part of $HGO_5$ reduced after 9 days of co-culture with cyanobacteria, indicating that $HGO_5$@CMlrA was stable during the process of incubation with *M. aeruginosa* (Figure S20).

Based on the above results, an inhibition mechanism of $HGO_5$@CMlrA against *M. aeruginosa* was proposed (Figure 5). First, intracellular changes were apparent from $HGO_5$@CMlrA treatment compared to control treatments (MlrA or $HGO_5$ treatment alone). The former also inhibited the expression levels of *rbc*L which is critical for Calvin cycle functioning in addition to MC-LR synthesis genes (*mcy*B, *mcy*G, and *mcy*D) to a much greater extent than did the MlrAs (CMlrA and PMlrA) or $HGO_5$ (Figure S24C) (Liu et al., 2020).

The concerted activities of $HGO_5$@CMlrA treatment would, eventually, lead to more serious changes in $LR_{in}$, cellular nucleoid regions, content overflowing, plasmolysis, and even cell death of *M. aeruginosa* cells (Figures 4A and 4E) (Liu et al., 2020). $HGO_5$@CMlrA can also inhibit Chl-a contents and $rETR_{max}$, resulting in reduced photosynthetic capacity and light energy use efficiency by *M. aeruginosa* (Figures 4B and 4D). However, $HGO_5$@CMlrA had almost no effect on $F_v/F_m$ and *psb*D, indicating that $HGO_5$@CMlrA could not inhibit the light energy conversion efficiency of PSII reaction centers, similar to that observed with $HGO_5$ treatment, but different from that observed in MlrA treatment (Figures 4C and S24A). The second major type of changes occurred extracellularly. $HGO_5$@CMlrA degraded $LR_{ex}$ that was released outside of cells. Furthermore, $HGO_5$@CMlrA maintained a weakly alkaline environment better than CMlrA, while $HGO_5$ did not affect culture pH (Figure 4F). A highly alkaline environment helps promote HMBs, wherein water pH can be as high as 10.5. Thus, $HGO_5$@CMlrA treatment can better help prevent the formation or maintenance of HMBs than CMlrA or PMlrA treatment alone (Huang et al., 2020; Huisman et al., 2018; Liu et al., 2020).

## Ecological safety of $HGO_5$@CMlrA composites

Interestingly, CMlrA and $HGO_5$ treatment promoted the expression levels of MC-LR synthesis genes (*mcy*B, *mcy*G, and *mcy*D) while $HGO_5$@CMlrA and PMlrA treatments inhibited their expression levels (Figure S24C). Previous studies have shown that both CMlrA and PMlrA can degrade MC-LR and inhibit *M. aeruginosa* growth, although CMlrA contains unknown HP and carries unknown ecological risks, thereby limiting its application (Liu et al., 2020). In addition, GOs also exhibit certain toxic characteristics (Wu et al., 2020; Seabra et al., 2014). Following the above results, an optimization strategy of $HGO_5$@CMlrA treatment combining CMlrA with $HGO_5$ was proposed (Figure 6A).

In this strategy, the adverse effects of CMlrA from HPs on ecological environments may be reduced by the removal of HPs while $HGO_5$ toxicity may be reduced by beneficial or harmless products (BPs) blocking the free active sites of $HGO_5$ during the synthesis of $HGO_5$@CMlrA. To validate this proposed strategy, a control experiment using $HGO_5$@CMBP was first established that was obtained by the immobilization of CMBP on $HGO_5$ (Figure 6B) was first established. The $HGO_5$@CMBP composite exhibited a 29.1% inhibition of *M. aeruginosa* after nine days of treatment. In contrast, the inhibition by CMBP was 61.6% and that of the directly mixed experimental group ($HGO_5$ + CMBP) was 59.4%. These results confirmed that $HGO_5$@CMBP reduced the toxicity of CMBP by possibly removing HPs in crude enzyme mixtures, while the toxicity of $HGO_5$ was reduced by BPs and MBP occupying the active sites of $HGO_5$ (Figure 6A). Similarly, the toxicity of CMlrA may be reduced by removing HPs during the preparation of $HGO_5$@CMlrA, while BPs and PMlrA may also reduce the toxicity of $HGO_5$ by occupying the active sites of $HGO_5$. Furthermore,

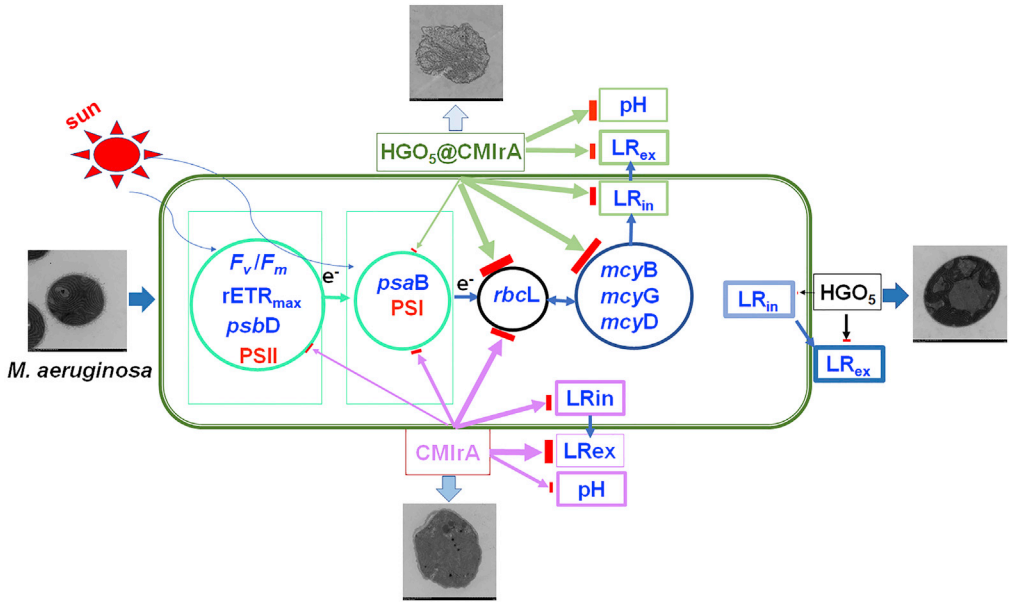


**Figure 5. Schematic illustrating intracellular and extracellular changes after treatment with $HGO_5$@CMIrA compared with control group treatments (CMIrA or $HGO_5$ alone) in *M. aeruginosa* cultures**

The lengths and widths of the red lines represent positive correlations between the inhibition intensity of various treatments and the various indices.

$HGO_5$@CMIrA treatment slightly inhibited or even promoted the growth of MC-non-producing algal species such as *Synechocystis* PCC6803 and the eukaryotic alga *Chlorella vulgaris* 1227 (Figure S25). These results indicate that $HGO_5$@CMIrA only targets the MC-producing algal species *M. aeruginosa* and exhibits higher application safety than $HGO_5$ and CMIrA.

A laboratory microcosm system was also used to assess the impact of $HGO_5$@CMIrA exposure on the prokaryotic and eukaryotic community structure and diversity in aquatic microcosms by 16 and 18S rRNA sequencing, respectively. Four alpha diversity metrics were evaluated, including the Shannon and Simpson indices that reflect community diversity and evenness, the Chao1 index that reflects species richness based on the estimated number of species, and the Pielou index that reflects species evenness (Figures 7A and S26A) (Zhang et al., 2020b).

The $HGO_5$@CMIrA exposure led to increases in the four alpha diversity indices compared to the CMIrA treatment, in addition to increases in the Simpson and Pielou index values of the prokaryotic community compared with the $HGO_5$ group. Thus, prokaryotic community diversity and evenness in the $HGO_5$@CMIrA group were higher than in the CMIrA group and the $HGO_5$ group (Figure 7A). Among the eukaryotic microbial communities, $HGO_5$@CMIrA exposure led to increases in the four alpha diversity metrics, indicating that eukaryotic community diversity, evenness, and species richness were all higher in the $HGO_5$@CMIrA treatment than in the other three treatments (Figure S26A). Thus, these results indicate that the diversity and evenness of prokaryotic and eukaryotic communities were significantly reduced by CMIrA treatment, but this negative impact could be alleviated after immobilization on $FGO_5$.

Principal coordinates analysis (PCoA) based on Bray-Curtis distances revealed variation in community β-diversity (i.e., species compositional variation) among prokaryotic and eukaryotic communities along with the first principal component (PC1) and the second principal component (PC2) (Figures 7B, 7C, and S26B). The species composition of the $HGO_5$@CMIrA treatment was significantly different from that in the other three treatments, indicating that the prokaryotic and eukaryotic community structures significantly shifted in the $HGO_5$@CMIrA treatment relative to the others. Moreover, some beneficial prokaryotic genera exhibited their highest relative abundances (RAs) in the $HGO_5$@CMIrA treatment compared to the other three treatments (Figure 7D). These taxa included *Acidovorax* which can degrade chlorobenzenes, diazotrophs (*Ideonella and Allorhizobium-Neorhizobium-Pararhizobium-Rhizobium*), *Dechloromonas,* and *Polynucleobacter* that can remove

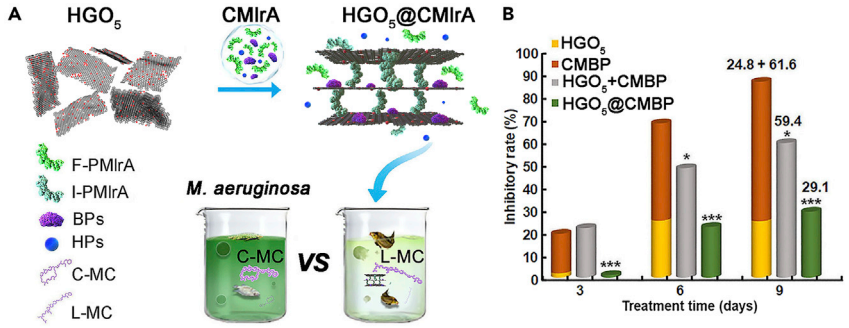


**Figure 6. Optimization strategy of $HGO_5$@CMIrA treatment that combines CMIrA with $HGO_5$**

(A) Schematic diagram showing the process of $HGO_5$@CMIrA preparation and application. F-PMIrA indicates free PMIrA, I-PMIrA indicates PMIrA immobilized on HGOs, BPs indicate beneficial or harmless products other than PMIrA within the CMIrA, and HPs indicate harmful products within CMIrA.

(B) Effects of $HGO_5$@CMBP composites on *M. aeruginosa* growth. Data are represented as mean ± SEM.

phosphorus, and *Sphaerotilus* that can remove heavy metals such as chromium and copper (Figure 7E(top)) (Monferran et al., 2005; Balázs et al., 2021; Petriglieri et al., 2021). In contrast, these beneficial genera exhibited low RAs in the other three treatment communities, indicating that the immobilization of CMIrA on $HGO_5$ can lead to safer aquatic microcosm conditions (Figure 7E(top)). The RAs of some prokaryotes involved in the degradation of MCs such as *Aeromonas* and *Sphingobacterium*, significantly increased by 15-fold and 50-fold, respectively, in the $HGO_5$@CMIrA and CMIrA treatments compared to the control and $HGO_5$ treatments (Figure 7E(down)). Notably, *Pseudanabaena* PCC-7429 within the *Cyanobacteria phyla* completely disappeared after the $HGO_5$@CMIrA and CMIrA treatments, but was still abundant in the $HGO_5$ and control groups, and thus demonstrates functions of CMIrA involved the removal of MCs and the inhibition of toxic cyanobacterial growth (Figure 7E(down)). Furthermore, some major genera in the eukaryotic communities, including *Ciliophora*, *Peritrichia,* and *Cyclidium*, exhibited significantly increased RAs in the $HGO_5$@CMIrA treatment, indicating that $HGO_5$@CMIrA treatment led to the maintenance of a better trophic structure for eukaryotic organisms compared to the other treatments (Figure S26D). Therefore, the immobilization of CMIrA on $HGO_5$ generally reduced the negative impacts of CMIrA on prokaryotic and eukaryotic communities. These results show that $HGO_5$@CMIrA is a more ecologically safe treatment for aquatic community composition than the use of free CMIrA and $HGO_5$. The effects of $CGO_3$@CMIrA treatment on prokaryotic and eukaryotic communities also exhibited similar trends (Figures S27 and S28), indicating that CMIrA immobilized on GOs can achieve the high ecological safety effects of GOs and CMIrA.

To further evaluate the safety of GOs@CMIrA ($HGO_5$@CMIrA and $CGO_3$@CMIrA) composites toward humans, cytotoxicity and lactate dehydrogenase (LDH) leak rate experiments were conducted with three human cell types (Figures S29–S32). The products of MC-LR after GOs@CMIrA treatment did not exhibit toxicity toward human cells compared to the control group. In contrast, MC-LR exhibited the highest observed toxicity toward the three human cell types. MC-LR was especially toxic toward normal hepatocytes (LO2) relative to the two other types of cancer cells. GOs@CMIrA treatments were also safe to human cells, while $HGO_5$ and $CGO_3$ exhibited certain levels of toxicity toward cells compared to the control. These results are consistent with previous reports showing that MC-LR and GOs are harmful toward human cells (Wang et al., 2021; Seabra et al., 2014).

## Conclusion

In this study, a unique $HGO_5$ was synthesized and screened with a high loading capacity for proteins that can degrade MCs. A new assembly mechanism was used relative to previously produced other modified GO derivatives, enabling the generation of the $HGO_5$ that can efficiently immobilize CMIrA and maintain the degradation activity of CMIrA against MCs, while simultaneously reducing the toxicity associated with CMIrA and $HGO_5$ alone. The $HGO_5$@CMIrA composite consequently simultaneously removed MCs and inhibited *M. aeruginosa* growth while exhibiting significantly better ecological and human safety compared to CMIrA or $HGO_5$. The method described here is universal and has potential for widespread application because it is low-cost and incorporates the easily available graphite as the raw material. $HGO_5$@CMIrA exhibited the best effects among the materials produced here. This proof-of-concept study may open new

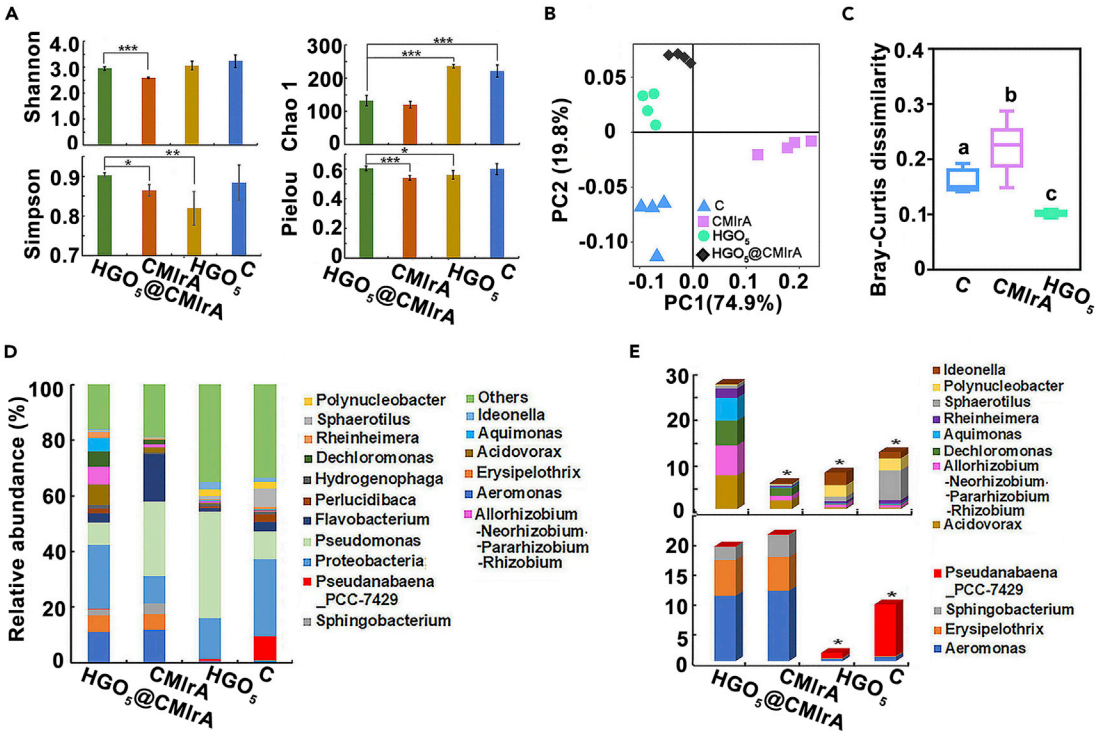


**Figure 7. Ecological safety of $HGO_5$@CMIrA treatment evaluated with effects on bacterial communities**

(A) Alpha diversity index values for bacterial communities.

(B) Principal coordinates analysis (PCoA) ordinations of variation in bacterial community composition across treatments.

(C) Bray-Curtis dissimilarities among treatment communities. Letters indicate statistically significant differences between different groups. Different letters in (C) represent significant differences ($p < 0.05$) between different treatments.

(D) Major bacterial genera of communities that exhibited relative abundances (RAs) > 1%.

(E) Major genera in the $HGO_5$@CMIrA treatment group that exhibited statistically significant differences relative to other groups (up), in addition to genera in both the $HGO_5$@CMIrA and CMIrA groups that exhibited significantly different abundances among the other two groups (down).

Asterisks (*, **, and ***) indicate statistically significant differences compared to controls ($p < 0.05$, $p < 0.01$, and $p < 0.001$, respectively). Data are represented as mean ± SEM.

avenues for GOs and MIrA, while comprehensively controlling HMBs and MCs pollution in water systems via the application of the proposed GOs@CMIrA.

## Limitations of the study

This study is fundamental research focused on the improvement of the utilization and security of MIrAs in MCs and *M. aeruginosa* treatment on the laboratory research scale. Some application technologies need further be developed for the widespread application of $HGO_5$@CMIrA in real water bodies in the future.

## STAR★METHODS

Detailed methods are provided in the online version of this paper and include the following:

- KEY RESOURCES TABLE
- RESOURCE AVAILABILITY
  - Lead contact
  - Materials availability
  - Data and code availability
- METHOD DETAILS
  - pMAL-c2X-*mlrA*-TB1 strains and *M. aeruginosa* FACHB 905
  - Preparation of HGO nanomaterials
  - Preparation of GO@MIrA composites
  - Characterization of GOs and GO@MIrA composites

- MCs degradation activities of CMlrA and $HGO_5$@CMlrA
- Density functional theory (DFT) simulation calculations
- Effects of GOs@CMlrA on cyanobacterial growth
- Effects of GOs@CMlrA on ecological microcosms
- GOs@CMlrA effects on human cells

- QUANTIFICATION AND STATISTICAL ANALYSIS
- ADDITIONAL RESOURCES

## SUPPLEMENTAL INFORMATION

Supplemental information can be found online at https://doi.org/10.1016/j.isci.2022.104611.

## ACKNOWLEDGMENTS

This work is supported by the National Natural Science Foundation of China (grant numbers 21877046, 21472061, 21976161, and 21272089), the Fundamental Research Funds for the Central Universities (grant numbers CCNU18ZDPY02 and CCNU16CG0002), and the Program of Introducing Talents of Discipline to Universities China (111 Program, B17019).

## AUTHOR CONTRIBUTIONS

L.F., H.L, C.C., and H.Q. designed the experiment. L.F. and H.L. wrote the article. H.L., C.C, L.Z, M.Y., Y.H., S.H., M.K., X.G., and Y.F. conducted the experiments. All the authors discussed the article.

## DECLARATION OF INTERESTS

The authors declare no competing interests.

Received: March 23, 2022
Revised: May 9, 2022
Accepted: June 8, 2022
Published: July 15, 2022

## REFERENCES

Al-Gaashani, R., Najjar, A., Zakaria, Y., Mansour, S., and Atieh, M.A. (2019). XPS and structural studies of high quality graphene oxide and reduced graphene oxide prepared by different chemical oxidation methods. Ceram. Int. *45*, 14439–14448. https://doi.org/10.1016/j.ceramint.2019.04.165.

Balázs, H.E., Schmid, C.A.O., Cruzeiro, C., Podar, D., Szatmari, P.M., Buegger, F., Hufnagel, G., Radl, V., and Schröder, P. (2021). Post-reclamation microbial diversity and functions in hexachlorocyclohexane (HCH) contaminated soil in relation to spontaneous HCH tolerant vegetation. Sci. Total Environ. *767*, 144653. https://doi.org/10.1016/j.scitotenv.2020.144653.

Chaudhary, K., Kumar, K., Venkatesu, P., and Masram, D.T. (2021). Protein immobilization on graphene oxide or reduced graphene oxide surface and their applications: influence over activity, structural and thermal stability of protein. Adv. Colloid Interface Sci. *289*, 102367. https://doi.org/10.1016/j.cis.2021.102367.

Chen, L., Shi, G., Shen, J., Peng, B., Zhang, B., Wang, Y., Bian, F., Wang, J., Li, D., Qian, Z., et al. (2017). Ion sieving in graphene oxide membranes via cationic control of interlayer spacing. Nature *550*, 380–383. https://doi:10.1038/nature 24044.

Dexter, J., McCormick, A.J., Fu, P., and Dziga, D. (2021). Microcystinase – a review of the natural occurrence, heterologous expression, and biotechnological application of MlrA. Water Res. *189*, 116646. https://doi.org/10.1016/j.watres.2020.116646.

Feng, J., He, H., Zhou, Y., Guo, X., Liu, H., Cai, M., Wang, F., Feng, L., and He, H. (2019). Design, synthesis and biological evaluation of novel inhibitors against cyanobacterial pyruvate dehydrogenase multienzyme complex E1. Bioorg. Med. Chem. *27*, 2413–2420. https://doi.org/10.1016/j.bmc.2019.01.021.

Hadi, J., and Brightwel, G. (2021). Safety of alternative proteins: Technological, environmental and regulatory aspects of cultured meat, plant-based meat, insect protein and single-cell protein. Foods *10*, 1226–1254. https://doi.org/10.3390/foods10061226.

Huang, J., Zhang, Y., Arhonditsis, G.B., Gao, J., Chen, Q., and Peng, J. (2020). The magnitude and drivers of harmful algal blooms in China's lakes and reservoirs: a national-scale characterization. Water Res. *181*, 115902. https://doi.org/10.1016/j.watres.2020.115902.

Huang, T., Xu, Z., Zeng, G., Zhang, P., Song, T., Wang, Y., Wang, T., Huang, S., Wang, T., and Zeng, H. (2019). Selective deposition of plasmonic copper on few layers graphene with specific defects for efficiently synchronous photocatalytic hydrogen production. Carbon *143*, 257–267. https://doi.org/10.1016/j.carbon.2018.11.029.

Huisman, J., Codd, G.A., Paerl, H.W., Ibelings, B.W., Verspagen, J.M.H., and Visser, P.M. (2018). Cyanobacterial blooms. Nat. Rev. Microbiol. *16*, 471–483. https://doi.org/10.1038/s41579-018-0040-1.

Hummers, W.S., and Offeman, J.R.R.E. (1958). Preparation of graphitic oxide. J. Am. Chem. Soc. *80*, 1339. https://doi.org/10.1021/ja01539a017.

Humphrey, W., Dalke, A., and Schulten, K. (1996). VMD: visual molecular Dynamics. J. Mol. Graph. *14*, 33–38. https://doi.org/10.1016/0263-7855(96)00018-5.

Klechikov, A., Yu, J., Thomas, D., Sharifia, T., and Talyzin, A.V. (2015). Structure of graphene oxide membranes in solvents and solutions. Nanoscale *7*, 15374–15384. https://doi.org/10.1039/c5nr04096e.

Krishnamoorthy, K., Veerapandian, M., Yun, K., and Kim, S.J. (2013). The chemical and structural analysis of graphene oxide with different degrees of oxidation. Carbon *53*, 38–49. https://doi.org/10.1016/j.carbon.2012.10.013.

Li, H., Ai, H., Kang, L., Sun, X., and He, Q. (2016). Simultaneous *Microcystis* algicidal and microcystin degrading capability by a single *Acinetobacter* bacterial strain. Environ. Sci. Technol. *50*, 11903–11911. https://doi.org/10.1021/acs.est.6b03986.

Li, P., Jin, Z., Fang, Z., and Yu, G. (2020). A surface-strained and geometry-tailored nanoreactor that promotes ammonia electrosynthesis. Angew. Chem. Int. Ed. *59*, 22610–22616. https://doi.org/10.1002/anie.202011596.

Li, P., Zhang, L., Wang, W., Su, J., and Feng, L. (2011). Rapid catalytic microwave method to damage *Microcystis aeruginosa* with $FeCl_3$-loaded active carbon. Environ. Sci. Technol. *45*, 4521–4526.

Liu, H., Guo, X., Liu, L., Yan, M., Li, J., Hou, S., Wan, J., and Feng, L. (2020). Simultaneous microcystin degradation and *Microcystis aeruginosa* inhibition with the single enzyme microcystinase A. Environ. Sci. Technol. *54*, 8811–8820. https://doi.org/10.1021/acs.est.0c02155.

Lu, T., and Chen, F. (2012). Multiwfn: a multifunctional wavefunction analyzer. J. Comput. Chem. *33*, 580–592. https://doi.org/10.1002/jcc.22885.

Luo, M., and Guo, S. (2017). Strain-controlled electrocatalysis on multimetallic nanomaterials. Nat. Rev. Mater. *2*, 17059. https://doi.org/10.1038/natrevmats.2017.59.

Marcano, D.C., Kosynkin, D.V., Berlin, J.M., Sinitskii, A., Sun, Z., Slesarev, A., Alemany, L.B., Lu, W., and Tour, J.M. (2010). Improved synthesis of graphene oxide. ACS Nano. *4*, 4806–4814. https://doi.org/10.1021/nn1006368.

Mehnati-Najafabadi, V., Taheri-Kafrani, A., and Bordbar, A.K. (2018). Xylanase immobilization on modified superparamagnetic graphene oxide nanocomposite: effect of PEGylation on activity and stability. Int. J. Biol. Macromol. *107*, 418–425. https://doi.org/10.1016/j.ijbiomac.2017.09.013.

Monajati, M., Borandeh, S., Hesami, A., Mansouri, D., and Tamaddon, A.M. (2018). Immobilization of *L*-asparaginase on aspartic acid functionalized graphene oxide nanosheet: enzyme kinetics and stability studies. Chem. Eng. J. *354*, 1153–1163. https://doi.org/10.1016/j.cej.2018.08.058.

Monferran, M.V., Echenique, J.R., and Wunderlin, D.A. (2005). Degradation of chlorobenzenes by a strain of Acidovoraxavenae isolated from a polluted aquifer. Chemosphere *61*, 98–106. https://doi:10.1016/j.chemosphere.2005.03.003.

Petriglieri, F., Singleton, C., Peces, M., Petersen, J.F., Nierychlo, M., and Nielsen, P.H. (2021). *Candidatus* Dechloromonas phosphatis" and "*Candidatus* Dechloromonas phosphovora", two novel polyphosphate accumulating organisms abundant in wastewater treatment systems. ISME J. *15*, 3605–3614. https://doi:10.1038/s41396-021-01029-2.

Reynosa-Martínez, A.C., Tovar, G.N., Gallegos, W.R., Rodríguez-Meléndez, H., Torres-Cadena, R., Mondragón-Solórzano, G., Barroso-Flores, J., Alvarez-Lemus, M.A., Montalvo, V.G., and López-Honorato, E. (2020). Effect of the degree of oxidation of graphene oxide on As(III) adsorption. J. Hazard Mater. *384*, 121440. https://doi.org/10.1016/j.jhazmat.2019.121440.

Seabra, A.B., Paula, A.J., Lima, R.D., Alves, O.L., and Durán, N. (2014). Nanotoxicity of graphene and graphene oxide. Chem. Res. Toxicol. *27*, 159–168. https://doi.org/10.1021/tx400385x.

Svirčev, Z., Lalić, D., Savić, G.B., Tokodi, N., Backović, D.,D., Chen, L., Meriluoto, J., and Codd, G. (2019). Global geographical and historical overview of cyanotoxin distribution and cyanobacterial poisonings. Arch. Toxicol. *93*, 2429–2481. https://doi.org/10.1007/s00204-019-02524-4.

Sun, B., Zhang, Y., Li, R., Wang, K., Xiao, B., Yang, Y., Wang, J., and Zhu, L. (2021). New insights into the colloidal stability of graphene oxide in aquatic environment: Interplays of photoaging and proteins. Water Res. *200*, 117213. https://doi.org/10.1016/j.watres.2021.117213.

Sun, P., Wang, K., and Zhu, H. (2016). Recent Developments in graphene-based membranes: structure, mass-transport mechanism and potential applications. Adv. Mater. *28*, 2287–2310. https://doi.org/10.1002/adma.201502595.

Tan, P., Bi, Q., Hu, Y., Fang, Z., Chen, Y., and Cheng, J. (2017). Effect of the degree of oxidation and defects of graphene oxide on adsorption of $Cu^{2+}$ from aqueous solution. Appl. Surf. Sci. *423*, 1141–1151. https://doi.org/10.1016/j. apsusc. 2017.06. 304.

Tsai, K.P., Uzun, H., Chen, H., Karanfil, T., and Chow, A.T. (2019). Control wildfire-induced Microcystis aeruginosa blooms by copper sulfate: Trade-offs between reducing algal organic matter and promoting disinfection byproduct formation. Water Res. *158*, 227–236. https://doi.org/10.1016/j.watres.2019.04.013.

Wang, H., Xu, C., Liu, Y., Jeppesen, E., Svenning, J.C., Wu, J., Zhang, W., Zhou, T., Wang, P., Nangombe, S., et al. (2021). From unusual suspect to serial killer: Cyanotoxins boosted by climate change may jeopardize megafauna. Innovation *2*, 100092. https://doi.org/10.1016/j.xinn.2021. 100092.

Wang, R., Li, J., Jiang, Y., Lu, Z., Li, R., and Li, J. (2017). Heterologous expression of *mlr*A gene originated from *Novosphingobium* sp. THN1 to degrade microcystin-RR and identify the first step involved in degradation pathway. Chemosphere *184*, 159–167. https://doi.org/10.1016/j.chemosphere.2017.05.086.

Wang, Y., Yang, R., Shi, Z., Zhang, L., Shi, D., Wang, E., and Zhang, G. (2011). Super-elastic graphene ripples for flexible strain sensors. ACS Nano. *5*, 3645–3650. https://doi.org/10.1021/nn103523t.

Wu, X., Wu, H., Gu, X., Zhang, R., Sheng, Q., and Ye, J. (2020). Effect of the immobilized microcystin-LR-degrading enzyme MlrA on nodularin degradation and its immunotoxicity study. Environ. Pollut. *258*, 113653. https://doi.org/10.1016/j.envpol.2019.113653.

Yu, Y., Zeng, Y., Li, J., Yang, C., Zhang, X., Luo, F., and Dai, X. (2019). An algicidal *Streptomyces amritsarensis* strain against *Microcystis aeruginosa* strongly inhibits microcystin synthesis simultaneously. Sci. Total Environ. *650*, 34–43. https://doi.org/10.1016/j.scitotenv.2018.08.433.

Zeng, S., and Kan, E. (2021). Adsorption and regeneration on iron-activated biochar for removal of microcystin-LR. Chemosphere *273*, 129649–129657. https://doi.org/10.1016/j.chemosphere.2021.129649.

Zhang, M., Wang, Y., Wang, Y., Li, M., Zhang, D., Qiang, Z., and Pan, X. (2019a). Efficient elimination and re-growth inhibition of harmful bloom-forming cyanobacteria using surface-functionalized microbubbles. Water Res. *161*, 473–485. https://doi.org/10.1016/j.watres.2019.06.035.

Zhang, M., Lu, T., Paerl, H.W., Chen, Y., Zhang, Z., Zhou, Z., and Qian, H. (2019b). Feedback regulation between aquatic microorganisms and the bloom-forming cyanobacterium Microcystis aeruginosa. Appl. Environ. Microbiol. *85*, e01362. https://doi.org/10.1128/AEM.01362-19.

Zhang, M., Mao, Y., Liu, G., Liu, G., Fan, Y., and Jin, W. (2020a). Molecular bridges stabilize graphene oxide membranes in water. Angew. Chem. Int. Ed. *59*, 1689–1695. https://doi.org/10.1002/anie.201913010.

Zhang, Q., Zhang, Z., Lu, T., Peijnenburg, W.J.G.M., Gillings, M., Yang, X., Chen, J., Penuelas, J., Zhu, Y.G., Zhou, N.Y., et al. (2020b). Cyanobacterial blooms contribute to the diversity of antibiotic-resistance genes in aquatic ecosystems. Commun. Biol. *3*, 737. https://doi.org/10.1038/s42003-020-01468-1.

Zhang, S., Zhang, X., Jiang, G., Zhu, H., Guo, S., Su, D., Lu, G., and Sun, S. (2014). Tuning nanoparticle structure and surface strain for catalysis optimization. J. Am. Chem. Soc. *136*, 7734–7739. https://doi.org/10.1021/ja5030172.

Zhuang, W., Quan, X., Wang, Z., Zhou, W., Yang, P., Ge, L., Hernandez, B.V., Wu, J., Li, M., Zhou, J., et al. (2020). Interfacial microenvironment for lipase immobilization: regulating the heterogeneity of graphene oxide. Chem. Eng. J. *394*, 125038. https://doi.org/10.1016/j.cej.2020.125038.

Zolezzi, C., Ihle, C.F., Angulo, C., Palma, P., and Palza, H. (2018). Effect of the oxidation degree of graphene oxides on their adsorption, flocculation, and antibacterial behavior. Ind. Eng. Chem. Res. *57*, 15722–15730. https://doi.org/10.1021/acs.iecr.8b03879.

## STAR★METHODS

### KEY RESOURCES TABLE

| REAGENT or RESOURCE | SOURCE | IDENTIFIER |
|---|---|---|
| Bacterial and virus strains | | |
| pMAL-c2X vector | New England Biolabs Inc. | Cat#E8000S |
| *Microcystis aeruginosa* FACHB 905 | Institute of Hydrobiology, Chinese Academy of Sciences (Wuhan, China) | FACHB-905 |
| *Synechocystis* sp. PCC6803 | Institute of Hydrobiology, Chinese Academy of Sciences (Wuhan, China) | FACHB-898 |
| *Chlorella vulgaris* FACHB 1227 | Institute of Hydrobiology, Chinese Academy of Sciences (Wuhan, China) | FACHB-1227 |
| pMAL-c2X-*mlrA*-TB1 strains | This paper | N/A |
| Chemicals, peptides, and recombinant proteins | | |
| Graphite | Maclin Biochemical Technology Co., Ltd. (Shanghai, China) | 7782-42-5 |
| $H_2SO_4$ | Sinopharm Chemical Reagent Co., Ltd. (Shanghai, China) | 7664-93-9 |
| $NaNO_3$ | Sinopharm Chemical Reagent Co., Ltd. (Shanghai, China) | 7631-99-4 |
| $H_2O_2$ | Sinopharm Chemical Reagent Co., Ltd. (Shanghai, China) | 7722-84-1 |
| $KMnO_4$ | Sinopharm Chemical Reagent Co., Ltd. (Shanghai, China) | 7722-64-7 |
| CGOs | Suzhou Crystal Silicon Electronic Technology Co., Ltd. (Suzhou, China) | 1034343-98-0 |
| $ZGO_0$ | Professor Heping Zeng of Sun Yat-Sen University | Huang et al. (2019) |
| FITC | Maclin Biochemical Technology Co., Ltd. (Shanghai, China) | 3326-32-7 |
| EDC | Aladdin industrial corporation (Shanghai, China) | 25952-53-8 |
| NHS | Aladdin Biochemical Technology Co., Ltd. (Shanghai, China) | 106627-54-7 |
| MES | Aladdin Biochemical Technology Co., Ltd. (Shanghai, China) | 4432-31-9 |
| MC-LR | Express Technology Co., Ltd. (Beijing, China) | 101043-37-2 |
| MC-RR | Express Technology Co., Ltd. (Beijing, China). | 111755-37-4 |
| MC-YR | Enzo Life Sciences, Inc. (Beijing, China) | 101064-48-6 |
| Critical commercial assays | | |
| CCK-8 Cell Proliferation and Cytotoxicity Assay Kit | Solarbio Co, Ltd | CA1210 |
| LDH activity detection kit | Solarbio Co. Ltd | BC0680 |
| RNeasy Plus Mini Kit | Qiagen, China | Qiagen 74136 |
| Transcriptor First Strand cDNA Synthesis Kit | Roche | 04896866001 |
| LightCycler 480 SYBR Green1 Master | Roche | 04887352001 |

(*Continued on next page*)

*Continued*

| REAGENT or RESOURCE | SOURCE | IDENTIFIER |
|---|---|---|
| Experimental models: Cell lines | | |
| LO2 (normal liver cell line) | ATCC | BJ-0432 |
| Huh7(liver cancer cell line) | ATCC | BJ-0271 |
| ACHN (renal cancer cell line) | ATCC | BJ-0172 |
| Oligonucleotides | | |
| Primer for 16s (338F) 5′-ACTCC TACGGGAGGCAGCAG-3′ | Zhang et al., 2020b | N/A |
| Primer for 16s (806R) 5′-GGACT ACHVGGGTWTCTA AT-3′ | Zhang et al., 2020b | N/A |
| Primer for 18s (528F) 5′-GCGG TAATTCCAGCTCCAA-3′ | Zhang et al., 2019a, 2019b | N/A |
| Primer for 18s (706R) 5′-AATC CRAGAATTTCACCTCT-3′ | Zhang et al., 2019a, 2019b | N/A |
| Primer for *psa*B-F CGGTGA CTGGGGTGTGTATG | Peng et al. 2017 | N/A |
| Primer for *psa*B-R ACTCGGTTTGGGGATGGA | Peng et al., 2017 | N/A |
| Primer for *psb*D-F TCTTCGGCATCGCTTTCTC | Peng et al., 2017 | N/A |
| Primer for *psb*D-R TCTTCGGCATCGCTTTCTC | Peng et al., 2017 | N/A |
| Primer for *rbc*L-F CGTTTCCCCGTCGCTTT | Peng et al., 2017 | N/A |
| Primer for *rbc*L-R CCGAGTT TGGGTTTGATGGT | Peng et al., 2017 | N/A |
| Primer for *mcy*B-F CCTACCGAGCGCTTGGG | Peng et al., 2017 | N/A |
| Primer for *mcy*B-R GAAAATCC CCAAAGATTCCTGAGT | Peng et al., 2017 | N/A |
| Primer for *mcy*D-F TTGACTAC ATAACCACCATCCTTC | Gao et al., 2013 | N/A |
| Primer for *mcy*D-R CTCCCTG GCAGTTTTGACAT | Gao et al., 2013 | N/A |
| Primer for *mcy*G AACGACA CGCCGCTCATTAC | Liu et al., 2020 | N/A |
| Primer for *mcy*G AACATCTG CCGAAGTGACTGC | Liu et al., 2020 | N/A |
| *mlrA* gene encoding MlrA from *Sphingopyxis* sp. C1 | Gene Bank | AB468058.1 |
| Recombinant DNA | | |
| Plasmid: pMAL-c2X-*mlrA* vector | This paper | N/A |
| Software and algorithms | | |
| QIIME2 software | Rideout et al., 2019 | https://qiime2.org/ |
| Multiwfn (A Multifunctional Wavefunction Analyzer) | Lu et al., 2012 | http://multiwfn.codeplex.com |
| Visual Molecular Dynamics (VMD) software program | Humphrey et al. (1996) | http://www.ks.uiuc.edu/Research/vmd |

## RESOURCE AVAILABILITY

### Lead contact

Further information and requests for resources should be directed to and will be fulfilled by the lead contact, Lingling Feng (fll708@mail.ccnu.edu.cn).

### Materials availability

Any materials generated in this study are being made available. The study did not generate new unique reagents or there are restrictions to availability.

### Data and code availability

The data are available upon request by contacting lead contact, Lingling Feng (fll708@mail.ccnu.edu.cn). No new code was generated during the course of this study.

## METHOD DETAILS

### pMAL-c2X-*mlrA*-TB1 strains and *M. aeruginosa* FACHB 905

The *mlrA* gene encoding MlrA from *Sphingopyxis* sp. C1 (Gene Bank: AB468058.1) was inserted into the pMAL-c2X vector with a maltose-binding protein (MBP) tag to construct the pMAL-c2X-*mlrA* vector, and the sequenced vector was transformed into *E. coli* K12 TB1 to obtain the recombinant pMAL-c2X-*mlrA*-TB1 strains. Briefly, the pMAL-c2X-mlrA-TB1 strains were cultured and then induced with 0.1 mM isopropyl-β-Dthiogalactoside (IPTG). By the way, CMlrA was the cell-free extracts.

*M. aeruginosa* FACHB 905 purchased from institute of Hydrobiology of the Chinese Academy of Sciences, cultivated in an artificial climate box to simulate natural conditions.

### Preparation of HGO nanomaterials

Nine types of graphene oxide ($HGO_1$-$HGO_9$) were synthesized using readily available and low-cost graphite powder ($HGO_0$) as the raw material based on Hummers' method (Hummers and Offeman, 1958; Marcano et al., 2010). The experimental design is shown in Figures 1A and Table S3. The HGOs exhibited different oxidation degrees and oxygen-containing functional group types (Table S2).

*Synthesis of HG $O_1$-$HGO_5$ by Method 1 (M1) based on Hummers' method* (Hummers and Offeman, 1958). Concentrated $H_2SO_4$ was first added to a mixture of graphite powder ($HGO_0$) and $NaNO_3$ in M1 (Table S3). Different amounts of oxidant $KMnO_4$ were then slowly added in the ice water bath. The reaction mixture was then heated to 98 °C for 15 min, and then maintained at room temperature for 10 min. Then, 30% $H_2O_2$ was added, followed by stirring for 1 h. The precipitate was collected by centrifugation and washed once using water and 5% HCl, followed by washing with water until achieving a neutral pH and then drying for later use.

*Synthesis of $HGO_6$-$HGO_9$ by Method 2 (M2) based on an improved Hummers' method* (Marcano et al., 2010). For synthesis using M2, a mixture of $H_2SO_4$ and $H_3PO_4$ was added to a mixture of $HGO_0$ with different dosages of $KMnO_4$ (Table S3). The reaction mixtures were then heated to 50°C, stirred for 12 h, and then cooled to room temperature for 10 min. Then, 30% $H_2O_2$ was added, followed by stirring for 2 h. The precipitates were then collected and washed as described above for M1.

### Preparation of GO@MlrA composites

MlrAs (CMlrA and PMlrA) and CMBP were prepared as previously described (Liu et al., 2020). Briefly, crude maltose binding protein (CMBP) was used as a control and was prepared from recombinant cells without *mlrA*. GOs@MlrA preparation was achieved using physical adsorption and covalent binding methods (Zhuang et al., 2020; Monajati et al., 2018).

For the physical adsorption method, 1 mg of GO ($HGO_5$ and other GOs) was dissolved into 1 mL of deionized water and ultra-sonicated for 30 min at room temperature. Then, the precipitate was collected by centrifugation, washed with phosphate buffer solution (PBS, 10 mmol $L^{-1}$, pH 7.4) three times, and resuspended in PBS to achieve a GO solution with a concentration of 0.625 mg $mL^{-1}$. MlrAs (5 mg $mL^{-1}$, 0.4 mL) were then added to the GO solution, followed by gentle shaking for 30 min at room temperature to initiate loading. The precipitate was subsequently collected by centrifugation, washed twice and resuspended with PBS for subsequent characterization and activity determination. The prepared composite was termed GOs@MlrA. The loading amount was calculated as follows:

$$\text{Protein loading amount}\left(\text{mg g}^{-1}\right) = \frac{C_0V_0 - (C_1V_1 + C_2V_2)}{m_0}$$

Where $C_0$ and $V_0$ indicate the initial concentrations and volumes of MlrAs, respectively. $m_0$ indicates the initial mass of GO used for enzyme loading. $V_1$ and $V_2$ indicate the volumes of centrifugated supernatants after loading and the volumes after washing with PBS, respectively. $C_1$ and $C_2$ indicate the protein concentrations in centrifugated supernatants after loading and after washing with PBS.

The covalent binding method comprised the dissolution of 1 mg GO into 1.6 mL of deionized water, followed by ultrasonication for 30 min at room temperature. 1-ethyl-3-(3-dimethylaminopropyl) carbodiimide hydrochloride (EDC dissolved in 0.5 mol $L^{-1}$ MES) and N-hydroxy-sulfosuccinimide sodium salt (NHS, dissolved in 0.5 mol $L^{-1}$ MES) were added to GO solutions to initiate activation of GO carboxyl groups for 30 min at room temperature. The loading process of MlrA on activated GO was the same as described above for the physical adsorption method.

## Characterization of GOs and GO@MlrA composites

Several methods were used to characterize the GOs and $GO_s$@CMlrA including scanning electron microscopy (SEM), atomic force microscopy (AFM), X-ray diffraction (XRD), X-ray photoelectron spectroscopy (XPS), Fourier transform infrared spectroscopy (FTIR), and Raman spectroscopy (RS).

The SEM instrument (JSM-7900F, JEOL, Japan) was equipped with an energy dispersive spectrometer (EDS, FlatQuad 5060F, Bruker, Germany) and TEM (HT-7700, Hitachi, Japan) to facilitate morphological characterization.

AFM images were obtained using a cypher ES atomic force field microscope (Oxford, England). The samples used for AFM characterization were deposited on a mica substrate. Specifically, $HGO_0$ and $HGO_5$ aqueous solutions were dispersed on mica substrates, then air-dried for 30 min prior to AFM characterization. AFM characterization of $HGO_5$@CMlrA and $HGO_0$@CMlrA was conducted in the aqueous solution.

XRD was performed to evaluate the crystal structures of the materials using a Rigaku D8/ADVANCE X-ray diffractometer (D8/ADVANCE, Bruker, Germany) with nickel-filtered Cu Kα radiation (λ = 0.15418 nm). The scan speed was 0.2 s per step with an angle range of 5–70°. The Bragg equation (di = nλ/2sinθ) was used to calculate the interlayer space ($d_i$) between nanosheets using an n = 1, an X-ray wavelength (λ) = 0.15418 nm, and the angle of diffraction as $\theta$. The average interlayer space was calculated according to the following equation:

$$\text{Average interlayer space} = \frac{d_1 \times P_1 + d_2 \times P_2}{P_1 + P_2}$$

Where $d_1$ indicates the interlayer space that is calculated based on the 2θ of the GO crystal plane (001, about 10.7°) and $d_2$ indicates the interlayer space calculated based on the 2θ of the graphite crystal plane (002, about 26°). $P_1$ and $P_2$ indicate the peak areas of the characteristic diffraction peaks of the 001 and 002 crystal planes, respectively.

XPS was conducted to analyze the elemental and functional group composition of the materials using a high-resolution X-ray photoelectron spectrometer (EscaLab 250Xi, ThermoFisher, USA).

RS was conducted to analyze the degree of meterial stacking order using a Raman microscopy system (LabRAM HR Evolution, HORIBA, France) with 532 nm laser excitation.

FTIR spectra were obtained on a Perkin-Elmer spectrometer Nicolet FT-IR 5700 instrument (Thermo, USA) using potassium bromide (KBr) as the background. CMlrA labeled with FITC was prepared to determine the distribution of CMlrA on the surface of $HGO_5$ using a Leica SP8 fluorescence microscope (Leica Microsystems trading co., Ltd., Shanghai, China). The excitation wavelength was set as 493 nm and the emission wavelength was set as 519 nm.

Material zeta potentials (Malvern Zetasizer Nano ZS90) were measured to evaluate their surface charges. Potentials were measured in samples at pH 7.4 using the same concentration 1 mg $mL^{-1}$ within water. In addition, the pH-dependence of zeta potentials were measured at pH 5.0, 6.4, 7.4, and 9.3.

All spectra were recorded under the same experimental conditions and all measurements were made in triplicate.

### MCs degradation activities of CMlrA and $HGO_5$@CMlrA

The MCs degradation activities of CMlrA and $HGO_5$@CMlrA were evaluated over time as we have previously described (Liu et al., 2020). Briefly, reaction mixtures that contained substrates (MCs) and enzymes (CMlrA or $HGO_5$@CMlrA) were prepared in 50 mmol $L^{-1}$ PBS, pH 7.0, and incubated at 25°C for 5 min. Then, 20% phosphoric-acid aqueous solution was added to terminate reactions. After centrifugation, residual MCs in the supernatants were detected using HPLC. One unit (U) of MlrA activity was defined as the quantity of enzyme that degrades 1.0 nmol of MC-LR per minute under the above conditions. The stability of the activities including thermal stability, pH tolerance, and storage stability were also evaluated as previously described. The activity recovery rates of enzymes were calculated by: (%) $=A_i/A_f$.

Where $A_i$ indicates the total activity of the GOs@MlrAs enzymes and $A_f$ indicates the total activity of free MlrAs used for loading.

### Density functional theory (DFT) simulation calculations

$HGO_0$ and $HGO_5$ models were constructed based on XPS analysis. For the $HGO_0$ model, $sp^2$ carbon atoms were contiguous with a hydroxyl group. For the $HGO_5$ model, part of the $sp^2$ carbon atoms were replaced by $sp^3$ carbon atoms, while hydroxyl and epoxides were randomly distributed inside the $HGO_5$ plane in addition to carbonyl and carboxyl groups that were distributed on the edge of the plane. Several lysines were predicted on the surface of MlrA in the predicted structure of MlrA by the Tencent AI Lab. Consequently, lysine was chosen to construct the models of $HGO_0$@CMlrA and $HGO_5$@CMlrA. Density functional theory (DFT) was then used to optimize the conformations of the models. The electrostatic surface potentials were analyzed with Multiwfn and drawn with the Visual Molecular Dynamics (VMD) software program to visualize the simulation configurations (Lu et al., 2012; Humphrey et al., 1996).

### Effects of GOs@CMlrA on cyanobacterial growth

Cyanobacterial cultures (*M. aeruginosa* FACHB 905, *Synechocystis* PCC6803, and *Chlorella vulgaris* FACHB 1227) were grown to the same cell densities of $3.75 \times 10^6$ cells•$mL^{-1}$ that corresponded to Chl-a contents of 0.5 μg•$mL^{-1}$ (Liu et al., 2020). These values correspond to the abundances of Cyanobacteria recorded during HMBs in Taihu Lake. Two milliliters of BG11 or other treatments, in addition to 100 mL of cyanobacterial cultures were placed in sterile 250 mL flasks. The treatment cultures were then investigated based on cellular morphologies, extracellular MC-LR ($LR_{ex}$) contents, intracellular MC-LR ($LR_{in}$) contents, the mRNA expression levels of genes, the maximum fluorescence quantum yields (*Fv/Fm*) of cells, the maximum relative electron transfer rates ($rETR_{max}$) of cells, Chl-a contents of cells, and media pH. The CMlrA + GOs treatment tested the effects of CMlrA plus GOs ($HGO_5$ or $CGO_3$) without immobilization treatment, while the GOs@CMlrA treatment tested the effects of GOs@CMlrA ($HGO_5$@CMlrA or $CGO_3$@CMlrA) composites obtained by immobilization treatment.

Chl-a content within cultures and culture media pH were determined at time points of 0, 3, 6, and 9 days using previously described methods (Liu et al., 2020). The inhibition rate (%) was calculated according to the following equation:

$$\text{Inhibition rate}(\%) = \frac{C_c - C_t}{C_c} \times 100\%$$

where *Cc* is the Chl-a content of the blank group and *Ct* is the Chl-a content of treatment group.

The maximum fluorescence quantum yield (*Fv/Fm*) and the maximum relative electron transfer rate ($rETR_{max}$) were determined at 24, 48 and 72 h using a fast chlorophyll fluorescence measurement on a pulse-amplitude modulation fluorometer (XE-PAM, Walz, Efeltrich, Germany).

Real-time fluorescent quantitative PCR (RT-qPCR) was used to assay the relative mRNA expression levels of genes (*psa*B, *psb*D, and *rbc*L) involved in photosynthetic pathways, in addition to genes (*mcy*B, *mcy*D, and *mcy*G) involved MC synthesis pathways at 24 and 48 h, using a LightCycler 96 PCR instrument (Roche, Switzerland). RT-qPCR methods were the same as previously described (Liu et al., 2020).

SEM, transmission electron microscopy (TEM), and fluorescence confocal scanning microscopy (FCSM) were used to observe cell morphologies after nine days of treatment, as described previously (Liu et al.,

2020). Samples treated for nine days were used to determine extracellular MC-LR (LRex) and intracellular MC-LR (LRin) contents, as described previously (Liu et al., 2020).

### Effects of GOs@CMlrA on ecological microcosms

The effects of GOs@CMlrA on aquatic community compositions were investigated as previously described (Zhang et al., 2020b). Briefly, freshwater samples were collected from a pond (30°17′59′′ N; 120°10′32′′ E) at the Zhejiang University of Technology in Hangzhou and then cultured for two days until stable under laboratory conditions before treatment. Then, 150 mL of cultured water samples were dispensed into 250 mL sterilized flasks for different treament groups. All groups were initialized at the same time and were grown under cool-white fluorescent light (46 μmol $m^{-2}$•$s^{-1}$) with a 12:12 light:dark photoperiod cycle and at 25 ± 0.5°C. Each group comprised four parallel replicates.

To investigate changes in aquatic community composition, 50 mL water samples from different groups were filtered through 0.45 μm pore diameter membranes to collect microbial cells after seven days of exposure. The nucleic acids of aquatic microorganisms were extracted using the cetyltrimethylammonium bromide (CTAB) method. The V3-V4 hypervariable regions of bacterial 16S rRNA genes were then amplified using polymerase chain reaction (PCR) and the primers 338F (5′-ACTCCTACGGGAGGCAGCAG-3′) and 806R (5′-GGACTACHVGGGTWTCTA AT-3′). In addition, the V4 hypervariable regions of eukaryotic 18S rRNA genes were PCR amplified using the primers 528F (5′-GCGGTAATTCCAGCTCCAA-3′) and 706R (5′-AATCCRAGAATTTCACCTCT-3′). The purified amplicons were then paired-end sequenced on an Illumina NovaSeq platform.

Raw sequencing data was quality-filtered to obtain clean data. Specifically, the QIIME2 software program was used to obtain clean data by denoising with Deblur to obtain amplicon sequence variants (ASVs). Taxonomy was assigned to ASVs using the q2-feature-classfier and comparison against the Silva 138 database. The Shannon and Richness α diversity indices were calculated using the R (version 4.0.3) vegan and picante packages. The Simpson index reflects the probability that the number of individuals obtained from two consecutive samples of a community belong to different species (Zhang et al., 2020b). PCoA plots were generated based on among-community Gower distances using the R package ggplot 2. Permutational multivariate analysis of variance (PERMANOVA; via ANOSIM tests and based on Gower distances, permutation = 999) tests were used to determine if community compositions differed between treatment and control groups.

### GOs@CMlrA effects on human cells

Three human cell lines including normal liver (LO2), liver cancer (Huh7), and renal cancer (ACHN) cell lines were used to evaluate cytotoxicity using a CCK-8 Cell Proliferation and Cytotoxicity Assay Kit (CA1210, Solarbio Co, Ltd). Each cell line was treated with 10 μg $mL^{-1}$ MC-LR, and sufficient GOs@CMlrA to completely degrade 10 μg $mL^{-1}$ MC-LR, in addition to an equivalent amount of CMlrA as GOs@CMlrA, an equivalent amount of GOs as GOs@CMlrA, or $P_{MC-LR}$ (a mixture including GOs@CMlrA and MC-LR). A1% methanol aqueous solution was used as the blank control since MC-LR was dissolved in a solution containing a 1% maximum concentration of methanol. In addition, the lactate dehydrogenase (LDH) leakage rate was evaluated using an LDH activity detection kit (BC0680, Solarbio Co. Ltd) after 48 h of treatment, as previously described (Liu et al., 2020).

## QUANTIFICATION AND STATISTICAL ANALYSIS

All experiments were performed in at least triplicate and the results shown are the means and standard deviations for three replicates. *t*-tests were used for statistical analysis of differences, and a $p < 0.05$ was considered statistically significant. Use origin software and excel software to make diagrams, and use photoshop CC software to combine graphics.

## ADDITIONAL RESOURCES

There are no additional resources need to be declared in this manuscript, additional requests for this can be made by contacting the lead contact.